

POLITECNICO DI TORINO



Corso di Laurea Magistrale in Ingegneria Aerospaziale

Tesi di Laurea Magistrale

Development of an Abel Transform Algorithm for Combustion Characterization and Data Analysis

Advisor

Prof. Dario Giuseppe Pastrone

Supervisor

M. Sc. Fernanda Winter

Author

Antonio D'Amato

Declaration of Authorship

Name: **D'Amato Antonio**

I hereby declare that this thesis is my own work prepared without the help of a third party. No other than the listed literature and resources have been used. All sources transferred literally or analogously to this work have been labeled accordingly.

Additionally, I hereby certify that this thesis has not been underlain in any other examination procedure up to the present.

24/04/18, *Antonio D'Amato*
.....
Date, Sign

Abstract

In order to develop and optimize a liquid rocket engine, the combustion process of the propellents combination GOX/CH_4 and GOX/H_2 are experimentally and numerically investigated at the Technical University of Munich to have a better understanding about performance for this propellant pair. The combustion processes are studied by means of an optical technique, called Chemiluminescence, that allows to detect the hydroxyl radicals OH^* emission spontaneously produced in the combustion chamber and use it as a flame reaction zone marker.

Because this optical diagnostics technique is a line-of-sight technique, in which each measured quantity is an integrated emission along each line-of-sight, emission local measurements are not directly possible but require a post-processing deconvolution of the measured intensities to obtain spatial information. One of the existing deconvolution techniques is the Inverse Abel Transform, applicable only in case the object under examination is axysimmetric and solvable only in approximate way. An overview of some methods of problem resolution is presented, including the Fourier Method presented by G. Pretzel (1991) choosen for this thesis. Based on it a Matlab algorithm for the Inverse Abel Transform has been developed. It has been tested with the known radial distribution functions taken from the literature. Once the algorithm was checked, it has been applied to images recorded from an ICCD camera to recover the emission radial distribution. Finally, the deducted results about the combustion process are to be discussed and validated finding confirmation in the literature and previous studies, demonstrating the validity of the code itself.

Contents

1	Introduction	1
1.1	Optical diagnostics	1
1.1.1	Emission Method	2
1.1.2	Optical setup	3
1.2	Comparison between numerical and experimental data issues	6
2	Abel transform	7
2.1	General explanation	7
2.2	Reconstruction errors	9
2.2.1	Measurement errors	9
2.2.2	Data preparation	11
2.3	Methods	13
3	Code	20
3.1	Code description	20
3.2	Test case	22
3.2.1	1D Case	22
3.2.2	2D Case	36
4	Experimental data	39
5	Results	44
5.1	Hydrogen	45
5.2	Methane	53
5.3	Experimental data vs numerical data	61
6	Conclusions & Outlook	63
7	Acknowledgments	64

A Appendix	68
A.1 Inverse Abel Transform code	68

List of Figures

1.1	Combustion chamber configuration [1]	3
1.2	Optical setup for emission imaging	4
1.3	Parallel rays collected by the camera [5]	5
2.1	Abel transform procedure [10]	8
3.1	Gaussian function radial distribution	22
3.2	Forward Abel of Gaussian function	22
3.3	Gaussian function: comparison between theoretical and reconstrued radial distribution	23
3.4	Gaussian function: relative error between theoretical and reconstrued radial distribution	23
3.5	Gaussian function radial distribution	24
3.6	Gaussian function projection with and without noise	24
3.7	Comparison between theoretical radial and reconstrued radial distribution for SNR=5	24
3.8	Relative error between theoretical radial and reconstrued radial distribution for SNR=5	24
3.9	Comparison between theoretical and reconstrued radial distribution for SNR=5 and $upf = 2$	25
3.10	Comparison between theoretical and reconstrued radial distribution for SNR=5 and $upf = 3$	25
3.11	Comparison between theoretical and reconstrued radial distribution for SNR=5 and $upf = 4$	26
3.12	Comparison between theoretical and reconstrued radial distribution for SNR=5 and $upf = 5$	26
3.13	Comparison between relative errors for different upf	26
3.14	Comparison between theoretical and reconstrued radial distribution for SNR=5 and $upf = 4$	27

3.15	Comparison between theoretical and reconstrued radial distribution for SNR=10 and $upf = 4$	27
3.16	Comparison between theoretical and reconstrued radial distribution for SNR=15 and $upf = 4$	27
3.17	Comparison between theoretical and reconstrued radial distribution for SNR=20 and $upf = 4$	27
3.18	Comparison between relative errors for different SNR	28
3.19	Cubic function radial distribution	29
3.20	Forward Abel of Cubic function	29
3.21	Cubic function: comparison between therotical and reconstrued radial distribution	29
3.22	Cubic function: relative error between theretical and reconstrued radial distribution	29
3.23	Cubic function radial distribution	30
3.24	Cubic function projection with and without a white Gaussian noise	30
3.25	Cubic function: comparison between theoretical and reconstrued radial distribution	30
3.26	Cubic function: relative error between theoretical and reconstrued radial distribution	30
3.27	Cubic function: comparison between theoretical and reconstrued radial distribution for SNR=5 and $upf=2$	31
3.28	Cubic function: comparison between theoretical and reconstrued radial distribution for SNR=5 and $upf=3$	31
3.29	Cubic function: comparison between theoretical and reconstrued radial distribution for SNR=5 and $upf=4$	31
3.30	Cubic function: comparison between theoretical and reconstrued radial distribution for SNR=5 and $upf=5$	31
3.31	Comparison between relative error for different upf	32
3.32	New test function radial distribution	33
3.33	Lateral projection of test function	33
3.34	New test function: comparison between theoretical and reconstrued radial distribution	33
3.35	New test function: relative error between theoretical and reconstrued radial distribution	33
3.36	New test function radial distribution	34
3.37	Lateral projection with and without a white Gaussian noise	34

3.38	New test function: comparison between theoretical and reconstrued radial distribution for SNR=20 and upf=4	34
3.39	New test function: relative error between theoretical and reconstrued radial distribution for SNR=20 and upf=4	34
3.40	Comparison between theoretical and reconstrued radial distribution for SNR=20 and upf=2	35
3.41	Comparison between theoretical and reconstrued radial distribution for SNR=20 and upf=3	35
3.42	Comparison between theoretical and reconstrued radial distribution for SNR=20 and upf=4	35
3.43	Comparison between theoretical and reconstrued radial distribution for SNR=20 and upf=5	35
3.44	Comparison between relative error for different <i>upf</i>	36
3.45	Recorded and recovered intensity images for Methane pressure 20 bar ROF = 2.2, 2.6, 3.0, 3.4	37
3.46	Comparison between the image and calculated intensity values for the axial position z=30 mm for ROF (a)2.2, (b) 2.6, (c) 3.0, (d) 3.4	38
4.1	Hydrogen ROF (a) 4.4 (b) 5.2 (c) 6.0 (d) 6.8	40
4.2	Hydrogen ROF (a) 4.4 (b) 5.2 (c) 6.0	41
4.3	Methane ROF (a) 2.2 (b) 2.6 (c) 3.0 (d) 3.4	42
4.4	Methane ROF (a) 2.2 (b) 2.6 (c) 3.0 (d) 3.4	43
5.1	Test Hydrogen 10 bar (a) ROF=4.4 (b) 5.2 (c) 6.0 (d) 6.8	45
5.2	Test Hydrogen 20 bar (a) ROF=4.4 (b) 5.2 (c) 6.0	46
5.3	Hydrogen: ROF=4.4 (a) P_{cc} =10 bar, (b) P_{cc} =20 bar	48
5.4	Hydrogen : normalized emission development for $ROF = 4.4$ and $P_{cc} = 10 \text{ bar} / 20 \text{ bar}$ along the axial direction for $r = 3 \text{ mm}$	48
5.5	Total OH^* radiance to change of pressure [5]	49
5.6	Hydrogen: P_{cc} =20 bar, ROF (a) 4.4 (b) 5.2 (c) 6.0	50
5.7	Normalized emission development for $P_{cc} = 20 \text{ bar}$ and $ROF = 4.4, 6.0$ along the axial direction for $r = 3 \text{ mm}$	50
5.8	Flame relative OH emission intensity as a function of injection velocity ratio and operating phase [25]	51
5.9	Hydrogen: emission radial profiles comparison for P_{cc} =20bar between test case ROF=4.4 and 6.0 at fixed axial position z=30 mm	52
5.10	Methane P_{cc} =10 bar (a) ROF=2.2 (b) 2.6 (c) 3.0 (d) 3.4	53

5.11 Methane $P_{cc}=20$ bar (a) ROF=2.2 (b) 2.6 (c) 3.0 (d) 3.4	54
5.12 Test Methane ROF=2.6 (a) 10 bar, (b) 20 bar	55
5.13 Methane : normalized emission development for $ROF = 2.6$ and $P_{cc} =$ 10 bar/ 20 bar along the axial direction for $r = 3mm$	56
5.14 Methane: comparison of radial normalized emission for axial position $z =$ 33mm and $ROF = 2.6$ for $P_{cc}=10$ bar/ 20 bar	57
5.15 Test Methane 20 bar ROF (a) 2.2 (b) 2.6 (c) 3.0 (d) 3.4	58
5.16 Methane: comparison normalized emission along axial direction for fixed lateral position $r = 3 mm$, $P_{cc}=20$ bar and $ROF=2.6, 3.4$	59
5.17 Profile of average heat flux at 1 mm distance from the hot gas wall along the axial position	60
5.18 Methane: emission radial profiles comparison for $P_{cc}=20$ bar between test cases $ROF=2.6$ and 3.4 at fixed axial position $z=30$ mm	60
5.19 Comparison numerical vs experimental	62

List of Tables

1.1	Measuring techniques for flame characterization [4]	2
1.2	Combustion chamber geometry [1]	4
4.1	Load points	39
5.1	Maximum Emission Intensity to change of pressure and propellant pair	44
5.2	Velocity ratio VR and flux ratio for different ROF and Hydrogen case	51
5.3	Methane: Velocity ratio VR and momentum flux ratio J for different ROF	57

Nomenclature

List of Symbols and Variables

A	[—]	Molecule
B	[—]	Molecule
Q	[—]	Molecule
M	[—]	Molecule in an excited state
M^*	[—]	Molecule
$h\nu$	[(a. u.)]	Photon
x	[mm]	Normal coordinate to the Combustion chamber axes
y	[mm]	Normal coordinate to the Combustion chamber axes
z	[mm]	Axial coordinate along the combustion chamber
y_c	[mm]	Center normal coordinate to the Combustion chamber axes
r	[mm]	Radial coordinate
R	[mm]	Maximum radius
R_k	[(a. u.)]	Radius of the k-th ring
δ_{jk}	[(a. u.)]	Intersecting length of each ray j with each shell k
f_k	[(a. u.)]	Radial distribution at the k-th ring
h_k	[(a. u.)]	Lateral distribution at the k-th ring
$f(r)$	[(a. u.)/mm ⁻³]	Radial distribution
$h(y)$	[(a. u.)/mm ⁻²]	Lateral distribution
$\epsilon(r)$	[(a. u.)/mm ⁻³]	Emission radial distribution
$I(y)$	[(a. u.)/mm ⁻²]	Intensity lateral distribution
G	[—]	Continuous Fourier transform of the intensities
J_0	[—]	Zero-order Bessel function of the first kind
Θ	[(a. u.)]	Angular direction
θ	[(a. u.)]	Angle
ϕ	[(a. u.)]	Angle

l	[(a. u.)]	Lateral coordinate
$c_{j,k}$	[-]	Coefficients of the k-th polynomial of j-order
f_n	[-]	Set of cosine functions
h_n	[mm]	Projection of the set of cosine functions
H	[mm]	Abel transform of the expansion series
N_l	[-]	Lower frequency limit
N_u	[-]	Upper frequency limit
μ	[-]	Mean of the distribution
σ	[-]	Standard deviation
P_{cc}	[bar]	Combustion chamber pressure
P_{c,O_2}	[bar]	Thermodynamic critical pressure of Oxygen
P_r	[-]	Reduced pressure
ROF	[-]	Oxygen to Fuel Ratio
VR	[-]	Fuel to Oxider velocity ratio
J	[-]	Fuel to Oxider momentum flux ratio

Abbreviations

TUM	Technische Universität München
UV	Ultraviolet range
GOX	Gaseous Oxygen
GH2	Gaseus Hydrogen
LOX	Liquid Oxygen
LH2	Liquid Hydrogen
GCH4	Gaseous Methane
OH	Hydroxyl Radicals ground state
OH*	Hydroxyl Radicals excited
ICCD	Intensified Charge Coupled device
SNR	Signal to noise ratio
upf	upper frequency
lof	lower frequency

Chapter 1

Introduction

1.1 Optical diagnostics

In order to develop and to optimize a liquid rocket engine, objective of test campaign is study the combustion process of the propellants combination oxygen/methane and oxygen/hydrogen. Referring to [1] *"this objective demand not only detailed understanding of all physical phenomena that determine performance but also validation of numerical tools. Since there is still insufficient knowledge about performance and heat release for this propellant pair, the Technical University of Munich has experimentally and numerically investigated the combustion process and heat transfer of rocket combustion chamber"*.

More details about the choice of this propellents are explained in the P. Difficile's Master thesis [2] and G. Laera's Master thesis [3]. The investigation of combustion process often does not allow the use of the conventional measurement techniques, so different techniques are required, one of these can be an optical technique in combustion diagnostics.

The use of the optical diagnostics is suitable to study the combustion because with their systems that have a non-intrusive nature allows to recover data during the combustion process without the insert of a measure instrument inside the combustion chamber that is hostile because of the high temperatures. However they have the disadvantage to be sensitive to the system perturbation, thus an appropriate optical technique must be chosen to provide benefit of accessibility and safety with accurate results.

Different measuring techniques exist depending to the characteristics of these and the quantities that want be measured.

They can be categorized in table 1.1

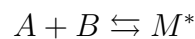
Measuring technique	Characteristics	Measurement results
PLIF	Flame radicals in reaction zone	Concentration of OH and CH
PLIF	Flame pollutant analysis	Concentration of NO , CO and SO_2
LII	Soot analysis in flame	Concentration profile of soot
LRS	Flame temperature	Profile of temperature
PIV	Flame velocity and mixing	Velocity field in flame
PDPA	Flame velocity and propagation	Velocity and size of particulates
Chemiluminescence	Flame radicals in reaction zone	Concentration of OH and CH

Table 1.1: Measuring techniques for flame characterization [4]

All this method are based on the fact that the radiation of the flames originates from the excited species that can be produced by three reactions: thermal collision with another molecule, chemical reaction of substances that form some species in the excited state and, finally, the absorption of a photon.

1.1.1 Emission Method

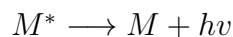
Referring to [5], in cold flames (below 2500 K) the radiation from excited molecules is observed to be much larger than the equilibrium radiation at that temperature. Such radiation is due to chemical excitation and *Chemiluminescence*. It consists in a production of light in a chemical reaction in which two substances A and B react to form the species M in the excited state:



This excited radicals or molecule can be deexcited by means of collision with another molecule:



or spontaneous emission of photon



The latter case corresponds just to *Chemiluminescence* and the emission occurs in the UV or visible range. It can occur in many processes which present unstable and intermediate species like combustion processes, hence for the current study the *Chemiluminescence method* is used to study the flame. It is used as a combustion diagnostic because the detected radiation is generated directly in the combustion chamber and the diagnostic does not have the necessity of expensive and laser instruments whose require maintenance [6]. There are various radicals that are generated in combustion process in which it is used the propellant combination oxygen/hydrogen, such as OH^* , and oxygen/methane, such as OH^* and CH^* . In this study only excited hydroxyl radical will be investigated. The reason is that "*its radiation is the most distinct radiation of flames in the UV and is often used as a flame marker because its spectrum around 310 nm is so far in the UV that thermal background radiation does not influence the measured signal*" [5].

The OH radicals detection offers a diagnostic for flame and combustion analysis due to its simplicity and non-intrusive nature.

1.1.2 Optical setup

The experimental setup used for the test campaign analyzed is based on the use of a modular single-element combustion chamber, consisting of two chamber segments of the 174 mm and 145 mm respectively and one nozzle with 20 mm of length. A shear coaxial injector element is present in which the fuel jet, respectively GCH_4 and GH_2 , envelops the oxygen jet GOX . The combustion chamber section is reported in fig. 1.1

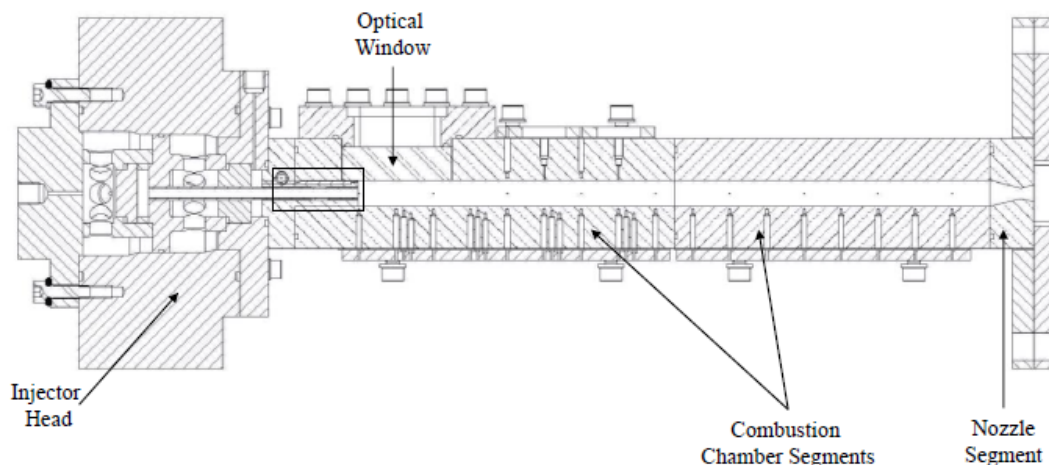


Figure 1.1: Combustion chamber configuration [1]

Where can be noted that, in the context of the optical diagnostics of the flame interaction in the near injection area the combustion chamber, is optically accessible by means of a quartz optical window of dimension $12 \times 40 \text{ mm}^2$.

The combustion chamber geometric features are reported in table 1.2

Length	290	[mm]
Width	12	[mm]
Height	12	[mm]
Throat height	4.8	[mm]
Contraction Ratio	2.5	[-]

Table 1.2: Combustion chamber geometry [1]

It is possible to see that it has a square cross section of $12 \times 12 \text{ mm}^2$, so the optical window is able to cover all combustion chamber height from wall to wall.

More details about the hardware description and the experiment setup can be found in P. Difficile's Master thesis [2] and in the paper of F.Winter et al. [1].

To detect the OH^* emission, a typical system consisted of an optical window, previously described, an ICCD (Intensified Charge Coupled Device) camera, a synchronization unit, a control software and a narrow band-pass filter placed in front of the lens to recover only the OH^* emission in a specific wave length.

The image 1.2 shows a optical setup pattern in which the camera is positioned on an optical test bench next to the test bench and the images of the flame passing through the optical window in the combustion chamber are reflected into the camera sensor by means of a planar mirror, which is positioned above optical window with a 45-degree angle to protect the camera from damage.

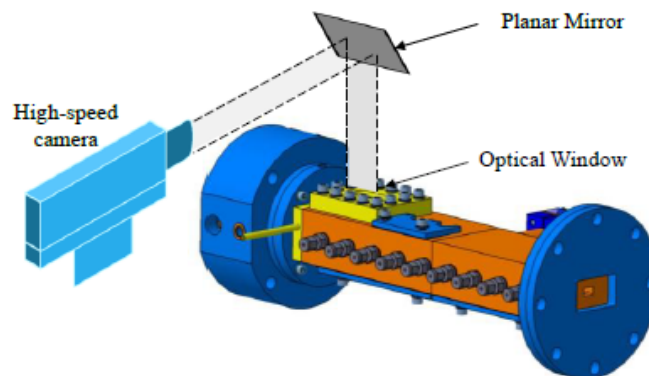


Figure 1.2: Optical setup for emission imaging

The chemiluminescence method is a line-of-sight technique, which measures the integrated light intensities, including signal contributions from both in front of and behind the focal plane of the lens. Because one of key requirements of the post-processing procedure as the Abel transform is that the lines of sight are single, non interfering lines, forming a parallel projection of the object under investigation, it can be obtained experimentally by ensuring that the camera is far away from the object. Considering a horizontal slice of the flame, the Fig. 1.3 represents the case of a camera infinitely far away from the flame, thus recording a beam of parallel rays and each pixel of the camera is associated with a single ray [5].

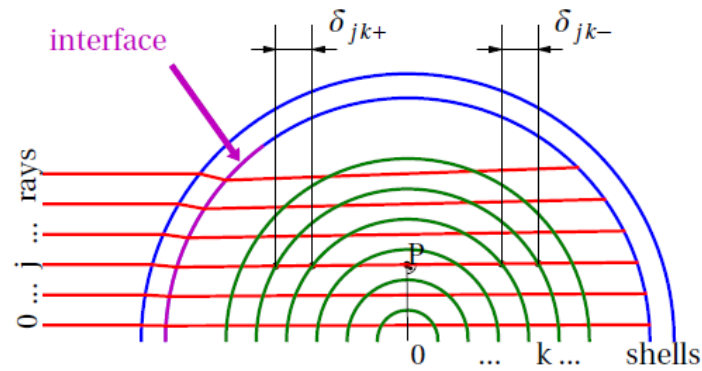


Figure 1.3: Parallel rays collected by the camera [5]

The camera record in every pixel the radiation integrated along the line-of-sight emitted from the chemically or thermally excited OH^* when they return to deexcited state, and because every pixel of the camera captures such quantity, a data matrix is obtained from each image in which the rows contain the integrated intensities for fixed lateral position in the flame to the change of axial position and the columns contain the integrated intensities for fixed axial direction position in the flame to the change of lateral position

This data acquisition method is faster and more resolutive than existing techniques, which require a separate measurement at each axial and lateral position. However, there are many disadvantages in the use of the measurements of flame radiation, as the fact that it is a line-of-sight integrated measurement and local measurements are not directly possible but require post-processing procedure, including a deconvolution in order to obtain spatially information. So an algorithm have to be developed to provide spatial representation of the OH^* emission measurements [7].

1.2 Comparison between numerical and experimental data issues

As well as with the optical diagnostic the flame is computed using a computational fluid dynamics (CFD) simulation performed by means of the commercial program Ansys Fluent [5]. However, referring to [1], because "*the numerical simulation is performed in 2D whereas the experimental quantities are measured along 3D lines of sight*" the comparison between experimental and numerical results is not possible. "*However, by means of a mathematical transformations, equivalent spatial profiles can be generated from each set of data. The conversion from the radial to the line-of-sight integrated quantities is commonly achieved by a so-called **Direct Abel transform**, while the reverse process by which the radial quantities are reconstructed from the line-of-sight integrated ones is known as **Inverse Abel transform***".

So, the experimental line-of-sight integrated quantities must undergo a deconvolution by application of the *Inverse Abel Transform* to recover the radial distribution of the emission and so to be able to compare with numerical simulation or the numerical results must be integrate to compare with experimental results.

Chapter 2

Abel transform

2.1 General explanation

The problem of reconstructing a two-dimensional radial distribution from measured projections or line integrals occurs in many different disciplines of science, physics and engineering such as plasma diagnostics. To have an estimation of the emission from a plane when an unknown function $f(r)$ cannot be measured directly but only the integrated quantities along lines of sight $h(y)$ are known, some inversion schemes can be used, one of these is the Abel Transform.

The necessary conditions to apply the Abel Transform is that the object under the observation has axial symmetry, e.g the axisymmetric distribution, and the value at the outer boundary and its derivative are zero [8].

Mathematically, the *Direct Abel Transform* of a radial quantity $f(r)$ in the line-of-sight integrated quantity $h(y)$ as a function of the distance y from the center line is given by:

$$h(y) = 2 \int_y^\infty \frac{f(r)r}{\sqrt{r^2 - y^2}} dr \quad (2.1)$$

while the *Inverse Abel Transform* is defined as:

$$f(r) = -\frac{1}{\pi} \int_r^\infty \frac{dh(y)}{dy} \frac{1}{\sqrt{y^2 - r^2}} dy \quad (2.2)$$

In flame and plasma diagnostics the Abel's equation relates the radial distribution of the emission coefficient $\epsilon(r)$ and the measured intensity $I(y)$, as can be seen in fig. 2.1, and

can be interpreted as a projection of a circularly symmetric function along a set of parallel lines of sight which are at distance y from the origin [9] .

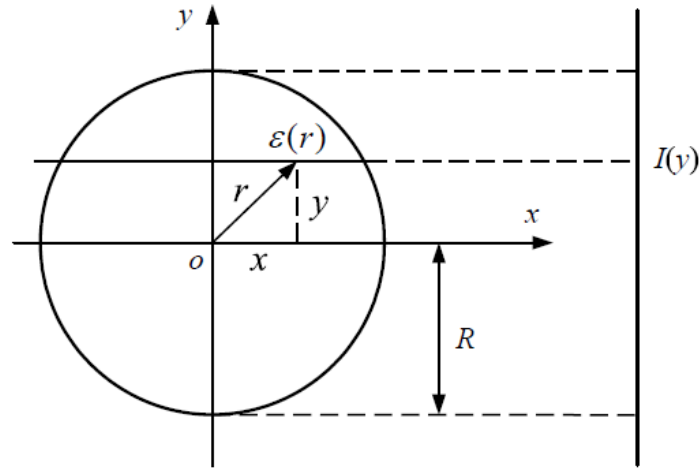


Figure 2.1: Abel transform procedure [10]

Because the Inverse Abel Transform contains the first derivative of measured data $I(y)$ with respect to y , but the measurements provide only a discrete set of data points, and because the singularity in the integral at the lower limit $y = r$, the process of estimation of the radial distribution $\epsilon(r)$ becomes ill-posed because small errors in the data can cause large errors in the reconstruction [9].

Furthermore, it means that the equation can only be solved in an approximate manner. Many methods and algorithms have been developed for solving the problem of Abel Inversion discretization whose, referring to [11], can be grouped into two principal categories:

- *Analytical methods*, whose fit the experimental data to an analytical function, which allows direct integration of the Abel inversion and avoids the discretization problem
- *Numerical methods*, whose transform the Abel inversion equation into a summation to allow processing of discrete sets of data.

Also, there are some methods whose combine the advantages of numerical and analytical methods.

2.2 Reconstruction errors

All these methods suffer of the same problems that can be produce in the inversion method the propagation of the errors and then some uncertainties in the determination of radial distribution from the measured data. The sources of errors can be:

- uncertainties in the Abel inversion
- uncertainties in geometrical factors
- uncertainties in input data

The Abel inversion errors arise from the fact that the radial distribution given by the Abel inversion differs from the real distribution, difference due both from the pretreatment and from the Abel inversion itself [11].

About geometrical factors, if the path length estimation in terms of determination of major radius and minus radius is incorrect, it introduces another errors in the inversion process, but definitely these errors can be neglected [12].

About the uncertainties in the input data, they require an post-processing procedure and can be classified in two main categories: measurement errors and errors due to data preparation.

2.2.1 Measurement errors

The main sources of error affecting the final results can be classified in:

- *Data noise*: Data noise and dynamics fluctuations of the flame can distort the radial distribution profile because of the dependence on the first derivative of integrated intensity data in the Abel inversion. To reduce this error, to smooth partially the noise and to have a better knowledge of what happens in the cumbustion, it can be taken each measurement after averaging over a large number of camera images. To obtain this average image, each recorded image in form of a matrix $D(i,j)$ is taken and for each (i,j) location is calculated the mean pixel intensity value between all the images. In this way, it is possible to obtain an average matrix of intensities.

This procedure does not totally eliminate data noise, so generally a technique to smooth the data must be included in the data treatment. There is a variety of techniques that can be used for smoothing, for example based on least-squares fitting, optical filtering of the noisy signal or smoothing with adjacent points [11]. However,

it can not be useful to smooth the measured profiles because one never knows whether that only reduces statistical noise or also changes the real information, and often the latter case is what happens. Furthermore, the error caused by incorrect smoothing cannot be estimated, so it is prenot even the order of magnitude, therefore it is preferable to use the unchanged measured profiles for the numerical reconstruction [13]

- *Calibration errors*: these are systematic errors that have the same effect on every measurement, the most contribution of whose are due to the absolute response calibration. These errors are due to the incorrect calibration during the image capture that produces distortions and non real values of flame emission.

These distortions are principally due to fact that there are many factors which influences the captured emission of the image, as lights and shadows caused by the external environment and the different sensitivity of each pixel that captures the light in different way.

To avoid these problems in the reconstruction, if the acquisition system is non correctly calibrated, it is necessary in a post-processing phase to apply to the image some corrections, such as the *Background correction* or the *Shading correction*. The *Background correction* considers the acquisition of a certain number of images by the ICCD camera with OH^* filter installed. These background images are then averaged by calculating the mean pixel intensity value across the set of images at each pixel location. Subsequently, the method requires the subtraction of the average background image from each of the individual images and then taking the average of the corrected images [7].

The *Shading correction* considers an image acquisition of the combustion chamber without the flame in way to have the brightness due to the external environment. Then the light inhomogeneity of this background image can be corrected and applied to the average image. In the experimental post-processing it was choosen to apply this last correction as presentend in the G. Laera's Master thesis [3]. However it was not obtained in time for the completion of this thesis so the images will be used without it.

To detect the brightness due to non uniform sensitivity of the ICCD camera sensor , an another technique can be considered which consists of the acquisition of an image with the lens covered, so the differences in the pixels response are only due to the sensitivity problem. Once obtained these corrections, they can be subtracted to the images.

Another possible distortion can be caused due to non correct position of the mirror

over the combustion chamber and the camera lens, which can happen by an unwanted movement of the optical bench or an inclination of the mirror. The last one can be corrected with the by post-processing. More details about these corrections are presented in the P. Difficile [2] and G. Laera's Master thesis [3].

2.2.2 Data preparation

Regarding to the uncertainties due to data preparation, they are mainly linked to the asymmetries in the flame image, incorrect detection of the center of flame and boundary estimation.

- **Influence of Asymmetries**

It should be noted that all the methods for numerical Abel inversion are capable to reconstruct only radially simmetrical function $f(r)$, but no one can be sure in practice if an arbitrary distribution is really radially symmetrical. In fact, the asymmetry can arise from the emission source or the detection process. When the asymmetry is due to the detection process, there is a constant source of asymmetry, e.g. experimental noise and difference in pixel response, which is not completely eliminated by pre-calibration of acquisition system or post-processing corrections and affects the two halves of measured projection $h(y)$ in a different way. The influence of this effect is more important for a small number of datapoints and the Abel inversion is highly sensitive to this asymmetry. An average profile have to be calculated summing for example the datapoints equidistant from the center of the distribution and dividing by 2 [11]. There is thus an influence of asymmetries on the reconstruction, but, although asymmetries by definition of Abel transform cannot be reconstructed, they do not introduce nonsense to the results.

However, they can be used to estimate the accuracy of results and so find a limit for the reconstruction errors. More details are expressed in [13].

- **Position of the flame center**

For accurate use of this symmetrization or if the assumption of axysimmetry is satisfied, the correct center of the flame must be detect to apply the Abel transform. The incorrect assumed central point has an influence on the quality of the reconstruction and its effects are much more severe in case of distribution with very pronounced peaks. Therefore can be advantageous to have a method to determine the approximately flame center.

One of these methods is reported by Pretzler [14] that calculates the y-coordinate of the center y_c as:

$$y_c = \frac{\sum_y y \cdot h(y)}{\sum_y h(y)} \quad (2.3)$$

e.g. as the ratio between the sum of all y-coordinates multiplied by the relative intensities and the sum of all intensities. This equation allows to yield the centre of the distribution with an accuracy better than 2% for all the simulated noisy profiles (1% for profiles with "realistic" noise), which is good enough for a satisfactory reconstruction.

This as other possible procedure are valid in the 1D case and must be extended to the 2D case of the image, e.g. must be applicated to the intensities profiles for each station along the axial direction, so a center line is finally found and can be used to symmetrize the image.

- **Influence of the boundary position**

Since the measured data, although symmetrical, are often subject to noise, the outer limits for the reconstruction procedure cannot be determined unambiguously. Referring again to [13], if the Abel condition at the outer boundary is satisfied, too narrow limits lead to too small values of the complete function that results because the measured profile $h(y)$ is setted to 0 at the limiting points, so the $f(r)$ give too small values if the $h(y)$ at the limiting points are greater than 0. On the other hand, too wide limits do not have any obvious effect. Then, to avoid errors of this kind the limits for the reconstruction should always be chosen too wide rather than too narrow.

However, because in the images the projection $h(y,z)$ has a non-zero value at the outer boundary due to a relatively small view field of ICCD camera and to the reflection on the mirror edge also in presence of correct calibration correction, the necessary condition to apply the Abel transform at this radius is not satisfied and then there is a deviation of the reconstrued results.

2.3 Methods

Several methods to solve numerically the Abel transform problem have been proposed in the years and are present in the literature.

Purpose of this section is to present the most used ones, the their limitations and explain the reasons that led to the choice of a well-defined method.

Matrix Method

Referring to Pretzler et al. [13], *"The oldest methods developed for numerically inverting the Abel equation (2.1) transform the measured data $h(y)$ linearly into the unknown distribution $f(r)$ using tabulated matrix. These matrices are calculated by discretizing either 2.1 or 2.2."*

There are different ways to calculate matrices which connect the measured data $h(y)$ to the local distribution $f(r)$. One of these is the onion peeling method, which assumes that the value of the local function $f(r)$ is constant in each of N rings around the simmetry axis. In this case the local data can be calculated iteratively from the outside to the inside via the equation 2.4:

$$f(r) = f_k = const, \quad \forall R_{k-1} > r \geq R_k \quad (k = 1, \dots, N) \quad (2.4)$$

By simple geometrical considerations one obtains N different values h_k of the projection $h(y)$:

$$h_k = \sum_{i=l}^k 2(\sqrt{R_{i-1}^2 - R_k^2} - \sqrt{R_i^2 - R_k^2}) f_i \quad (2.5)$$

where M is the number of measured points and

$$a_{j,i} = 2\sqrt{r_i^2 - y_j^2} \quad (2.6)$$

All quantities in the summatory are the matrix a_{ik} which is triangular and can easily be inverted to obtain the values f_k out of the measured data points h_k [13]

However, this method calculating the local data going from outside to the inside does not work well with the noise images, because in the reconstructed image it increases progressively towards the center.

Fourier-Hankel Method

This method commonly used for calculation of the inverse Abel transform is based on the Fourier transform of the projection data and then on the inverse Hankel transform of them. Referring to [15] taking the Fourier transform of intensity and changing the variable of the integration to polar coordinates, it can be proved that such Fourier transform of $I(y)$ is equal to the zero-order Hankel transform of $\epsilon(r)$. So, the emission coefficient can be recovered from the inverse Hankel transform

$$\epsilon(r) = \frac{1}{2\pi} \int_0^\infty G(\omega)\omega J_0(\omega r)d\omega \quad (2.7)$$

where $G(\omega)$ is the continuous Fourier transform of the intensities and

$$J_0(\omega r) = \frac{2}{\pi} \int_r^\infty (x^2 - r^2)^{-1/2} \sin(\omega x) dx \quad (2.8)$$

is the zero-order Bessel function of the first kind. Indicating with $\Delta\omega = \alpha\pi/R$, the equation which expresses the emission coefficient can be discretized as :

$$\epsilon(r) = \frac{\alpha^2\pi}{2nR} \sum_{k=1}^n kG(\alpha k) J_0\left(\frac{\alpha k r \pi}{n}\right) \quad (2.9)$$

in which:

$$G(\alpha k) = \sum_{j=-n}^{n-1} I(x_j) \cos\left(\frac{\alpha j k \pi}{n}\right) \quad (2.10)$$

More details are presented in [15] This method can greatly reduce the computation time using the fast Fourier transform (FFT) and avoid the singularity in the inverse Abel transform. However, in accordance with Dribinski and all. [16] this method however magnifies the experimental noise and also produces artificial structures when reconstructing images with high-intensity sharp features that extend through the entire reconstructed image, causing a reduction in resolution and in signal-to-noise ratio. Furthermore the Fourier-Hankel method cannot yield reasonable results for small sets of data [10].

Convolution method

This method is what normally used for asymmetrical geometry, but can be extended to the case of asymmetrical distribution.

An asymmetrical distribution $f(r,\phi)$ can be obtained utilizing light transmission if the projections $h(l,\Theta)$ is known for different directions Θ [13].

The analytical relationship between them is given by the inverse Radon transformation

$$f(r,\phi) = \frac{1}{2\pi^2} \int_0^\pi \left(\int_{-\infty}^{+\infty} \frac{1}{r\cos(\theta - \phi) - l} \frac{dh(l,\Theta)}{dl} \right) d\Theta \quad (2.11)$$

which is a general form of Inverse Abel transformation.

There are several methods known as computer tomography to solve numerically this equation, one of these is the convolution method.

It is possible to extend and adapt the concepts of such successful method to the case of radial symmetry.

It can be shown that for asymmetrical distributions, the $f(r,\phi)$ can be transformed into

$$f(r,\phi) = \int_0^\pi \left(\int_{-\infty}^{+\infty} h(l,\Theta) q_A(r\cos(\Theta - \phi) - l) dl \right) d\Theta \quad (2.12)$$

which is a convolution of the measured data $h(l,\Theta)$ with the convolving function [13] :

$$q_A(s) = -2 \int_0^{A/2} F_A(u) \sin(2\pi us) du \quad (2.13)$$

In the case of radial symmetry can be simplified as:

$$f(r,\phi) = \int_0^\pi \left(\int_{-\infty}^{+\infty} h(y) q_A(r\cos\Theta - y) dy \right) d\Theta \quad (2.14)$$

More details about the method are contained in literature and in the work of Pretzler et al. [13]. Finally they have concluded that the convolution method for the case of radial symmetry gives bad results, worse than those of the other methods proposed here, and it has longer calculation times.

Interpolating Method

Most of the methods are based on an interpolation of either the measured data $I(y)$ or the unknown local function $f(r)$. In the latter case the unknown function is then integrated and compared to measured data [8]

- **h-interpolation Method**

Many methods to solve the inverse Abel transform problem are based on smooth the noise or interpolate the measured function $h(y)$ by means of simple functions which allow the differentiation and the integration in the Inverse Abel transform to be performed analytically.

One of these methods is for example using a cubic spline interpolation. According to Pretzler et al. [13], every two adjacent data points are connected by a polynomial of the third degree with the same first and second derivative of the next polynomial for the next interval at the connecting point. With this four conditions for each polynomial, it is possible to calculate the four coefficients whose allow to represent the measured function $h(y)$ with N measured points by $(N-1)$ polynomials:

$$h(y) = P_k(y) = \sum_{j=0}^3 c_{j,k} y^j \quad (2.15)$$

$$\forall y : y_k \leq y \leq y_{k+1} \quad , \quad k = 0, \dots, N-2$$

In this form the measured function can be derived analytically and insert into radial distribution equation:

$$f(R_i) = -\frac{1}{\pi} \sum_{n=i}^{N-2} \sum_{j=0}^2 \alpha_{j,n} \int_{R_n}^{R_{n+1}} \frac{y^j}{\sqrt{y^2 - R_i^2}} dy \quad (2.16)$$

The integrals are solved analytically, allowing to calculate the function $f(r)$ at N discrete points $r = R_i$.

More details are described by Pretzler et al. [13] , who have shown that in the case of profiles with "many" data points this method is not suited and should not be used.

- **f-interpolation Method**

It is possible to interpolate the unknown radial distribution $f(r)$ and not the measured projection $h(y)$ with functions that have an analytical solution of the direct Abel transform. Chosen such set of functions, the f - interpolation method suggested by Pretzler et al. [13] allows to interpolate the local distribution $f(r)$ with polynomials of third degree:

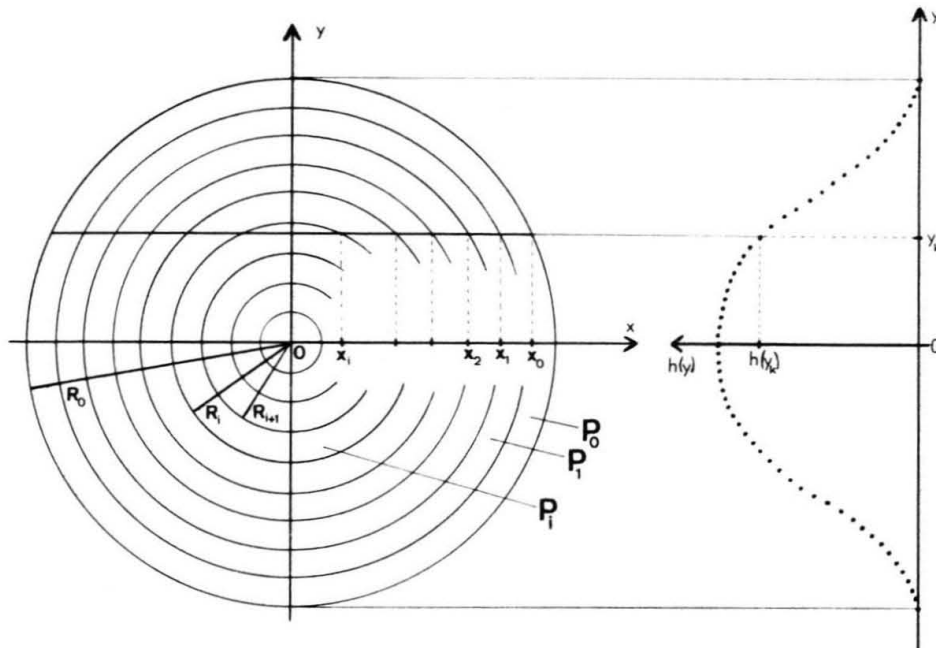
$$f(r) = P_i(r) = A_i r^3 + B_i r^2 + C_i r + D_i \quad (2.17)$$

with:

$$R_i \geq r \geq R_{i+1}$$

where R_i is the radius at the position i and $1 \leq i < M$, with M number of polynomials.

The axysimmetric zone is divided in some rings, for each of them a polynomial $P_i(r)$ is introduced to describe the radial distribution $f(r)$



Some boundary conditions have to be imposed to recover the unknown coefficients A_i, B_i, C_i, D_i and they are that $P_i(R_{i+1}) = P_{i+1}(R_{i+1})$ and $P_i(R_{i+2}) = P_{i+1}(R_{i+2})$, e.g. that every polynomial is assumed to have the same value of the near polynomials at limiting points $r = R_i$ and $r = R_{i+1}$. Another two conditions are imposed

at the outer boundary, e.g. that $P_M(R_{M+1}) = 0$ and $P'_M(R_{M+1}) = 0$ and one at the center, e.g. $P'_1(0) = 0$. In this way it is possible to calculate all coefficients for every polynomial with a least squares criterion and hence the complete function $f(r)$.

The f -interpolating method shows good results and is very efficiently programmable. More detail about this method are presented in [13] and [8]

- **Fourier Method**

The problem with many methods of numerical Abel inversion is that they work gradually from the periphery to the centre of the flame, and thus the errors of measurements of the outer parts have an influence on the results in the central region and make these uncertain. So, we look for numerical methods that perform the calculation in one step, e.g. non iterative calculation [13].

One of these is the *Fourier Method* based on the work of *Georg Pretzler* [14] is what it has been decided to use. In an approach of this type, very different from the previous, referring to [14], *the unknown radial distribution $f(r)$ is expanded in a series similar to a Fourier series:*

$$f(r) = \sum_{n=N_l}^{N_u} A_n f_n(r) \quad (2.18)$$

with unknown amplitudes A_n , where $f_n(r)$ is a set of cosine functions, e.g.

$$f_0(r) = 1 \quad (2.19)$$

$$f_n(r) = 1 - (-1)^n \cos(n\pi \frac{r}{R}) \quad (2.20)$$

The direct Abel transform of the equation 2.18 is:

$$H(y) = 2 \sum_{n=N_l}^{N_u} A_n \int_y^R f_n(r) \frac{r dr}{\sqrt{r^2 - y^2}} \quad (2.21)$$

In this equation, each integral

$$h_n(y) = \int_y^R f_n(r) \frac{r dr}{\sqrt{r^2 - y^2}} \quad (2.22)$$

cannot be solved analytically but are calculated numerically and stored in a specific file. Through the amplitudes A_n are unknown, it can consider that at each of the N points $y = y_k$ the function $H(y, A_n)$ should approximate the measured data $h(y_k)$.

This declaration can be written as a least squares criterion:

$$\sum_{k=1}^N (H(y_k) - h(y_k))^2 \longrightarrow \min \quad (2.23)$$

The insertion of the expression of $H(y)$ in this equation and the resolution with respect to the unknown amplitudes A_n leads to

$$\sum_{n=N_l}^{N_u} A_n \sum_{k=1}^N (h_n(y_k) h_m(y_k)) = \sum_{k=1}^N (h(y_k) h_m(y_k)) \quad (2.24)$$

$$\forall m : N_l \leq m \leq N_u$$

The equation system yields the amplitudes A_n which inserted in the expression of $f(r)$ return the resulting radial distribution.

Referring to [13], the Fourier method has some advantages over the other numerical processes. They can be schematized as:

- this method do not work from the periphery to the centre, so the errors of measurements of the outer parts do not have an influence on the results in the central region.
- it is derivative-free because of the transformation of the whole problem from the r- to the y-space
- neither smoothing or any other kind of pre-treating of the measured data $h(y)$ is necessary. Following this method, the numerical inversion can be used as a noise filter by choosing the lower and upper frequency limits N_l , and N_u . This can be supported by adaption of the exact form of the model functions $f_n(r)$ to the given physical conditions. Then the upper limit N_u can be chosen low enough for an efficient low-pass filtering because the reconstruction almost entirely depends on the low-frequency components: a higher upper limit translates in a better reconstruction, but it is not possible to go too far with the N_u because the method low-pass filtering is lost.
- Because of these characteristics, it give the best results between the proposed method, even better than the f -interpolating method. It was also chosen because it is easily programmable
- Furthermore, the number of expansion cosine affects also the computation time: low upper frequency translates into low computational time

Chapter 3

Code

3.1 Code description

Based on the Abel inversion method described by George Pretzler and partially on the Carsten Killer's work [17] a Matlab-algorithm was developed .

The goal of this chapter is the description of the code and its functionality. First note that the Fourier Method chosen allows to recover the one-dimensional radial distribution $f(r)$ once available the one-dimensional projection $h(y)$.

However, the images recovered by the CCD camera are represented by 2D matrices, in whose every column represents a lateral projection for a well-defined station along the flame axial direction, therefore this procedure has to be applied to every station along the axial direction, extending the method to a 2D case.

Based on what has been said, in the first part of the code the intensity values are extracted from the image of the CCD camera as 2D matrix, in which at each index i,j corresponds the intensity captured from a well-defined pixel i,j .

Identifying with z the coordinate along the image axial direction, that coincides with the flame axial direction, and with y the coordinate along the image radial direction, in such matrix every rows contain the integrated intensities for a fixed pixel radial position y to change of the pixel axial position z in the flame and every columns contain the integrated intensities for a fixed pixel axial position z to change the pixel lateral position y .

Note that such intensity values are captured from the ICCD camera pixels on all optical window of dimensions 40 mm x 12 mm, that in lateral direction cover the entire height of the combustion chamber, and contain the contributions of both the upper and lower part of the flame.

The vector y , which identify the radial pixels coordinates, is defined as equidistant values ranging from 0 to 12, where 0 mm is the down wall of the combustion chamber and 12

mm is the distance of the upper combustion chamber wall from the down one. Instead the vector z represents the axial pixels coordinates, varying from 0 to 40, where 0 mm is the injection plane and 40 mm is the length of the optical field. Both this vectors are in number equal to a pixels number respectively in radial and axial direction

However, since the Abel transform can only be applied if the object under observation has cylindrical axisymmetry, only half of the image in radial direction has to be taken in consideration. Because of the asymmetries that are inevitably present in the upper and lower half of image, an average image must be calculated using the intensity datapoints equidistant from the flame center.

To make this symmetrization, the flame center should be detected and it should be performed station by station along the axial direction with one of the possible techniques from the literature. However, in the code, it has been assumed that the center is located exactly at half of the image height and that it is constant along the axial direction.

Consequently, a radius vector r is defined as a vector of equidistant values in radial direction, in number equal to intensity values number of this average image in radial direction and associated to them, ranging from 0 to 6, where 0 mm corresponds to the flame center and 6 mm to the combustion chamber wall distance from the flame center, that is theoretically also equal to the maximum radius.

However, computationally the effective maximum radius will be posed equal to a slightly bigger value, $R = 6.001 \text{ mm}$, to avoid the Not-a-Number value when the limits of Abel transform integral are the same, e.g. $y = R$.

With the known z coordinates along the flame axial direction and the known r coordinates along the flame radial direction, the Fourier method is implemented in the code central part and extended to the 2D case applying it by means of a Matlab cycle *for* to every intensity profile along lateral direction to change of the station along the axial direction. In this way every radial distribution profile is individually recovered and the overall radial distribution image is obtained.

Finally, once it is recovered, the direct Abel transform is reapplied to check the code and the goodness of the reconstruction for looking if the new projection image is equal or similar to the recorded image from ICCD camera.

3.2 Test case

3.2.1 1D Case

Once written, to check the code it is always desirable to use some test cases from literature for whose the theoretical radial profiles $f(r)$ and the corresponding lateral emission profiles $h(y)$ are known.

Such functions are reported for example in the work of M.J. Buie et al. [18], H. Fulge et al. [8], George Chan et al. [19]. Three test cases are being considered because they are of particular interest both for the flame shape and for the reconstruction difficulties.

Test case 1

Referring to [8], the first taken test case is an off centered Gauss function, due to the fact that most local distributions in plasma facilities are expected to have a Gaussian shape. Such function can be written as:

$$f(r) = \frac{1}{\sigma\sqrt{2\pi}} \left(\exp(-1/2(\frac{r-\mu}{\sigma})^2) + \exp(-1/2(\frac{-r-\mu}{\sigma})^2) \right) \quad (3.1)$$

The mean or expectation of the distribution μ and the standard deviation σ are chosen to be $\mu = 0.3$ and $\sigma = 0.2$ to obtain an off centered function, while r is a vector of equidistant values taken from 0 to 1.

The forward Abel transform of this function can only be calculated numerically.

The theoretical radial and its numerical lateral profiles are presented in the figures 3.1 and 3.2

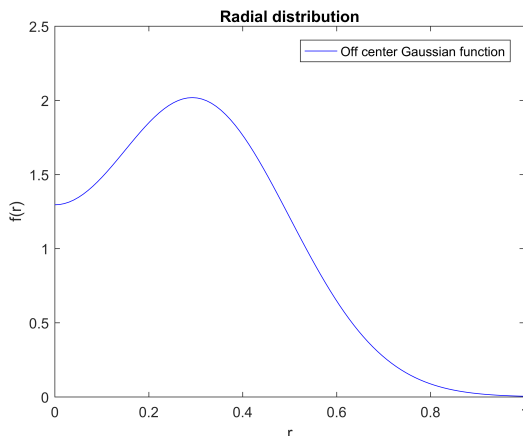


Figure 3.1: Gaussian function radial distribution

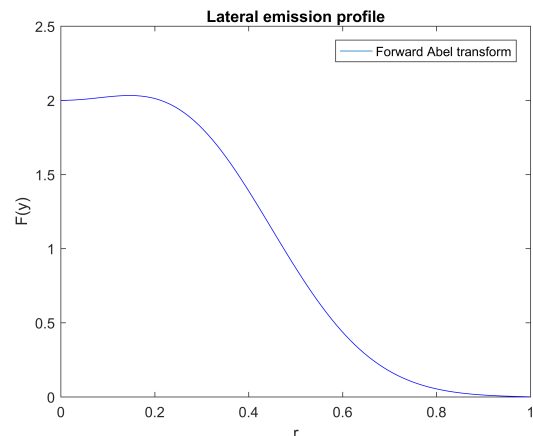


Figure 3.2: Forward Abel of Gaussian function

Now it is possible to apply the code to the lateral emission profile and check if the theoretical radial distribution is recovered quantifying the differences between such note function and the resulting radial distribution after the code application. The results obtained with an $upf = 10$ are shown in figs. 3.3 and 3.4

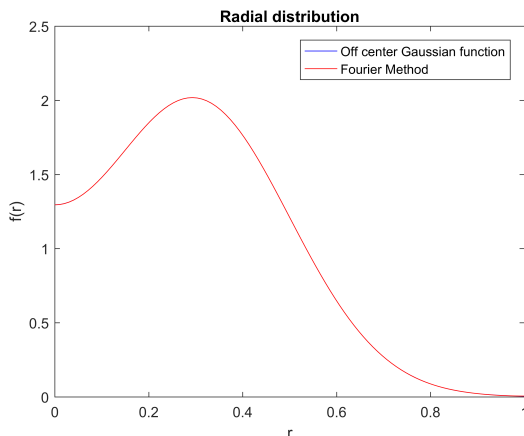


Figure 3.3: Gaussian function: comparison between theoretical and reconstrued radial distribution

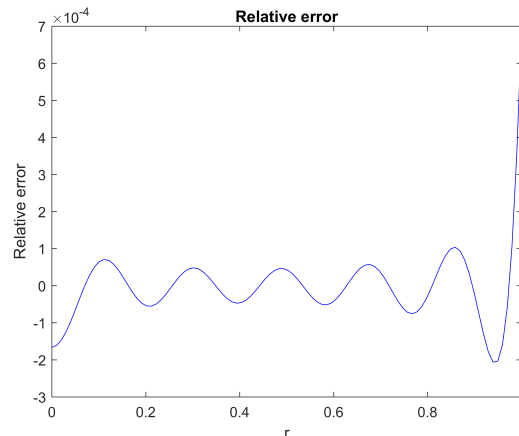


Figure 3.4: Gaussian function: relative error between theoretical and reconstrued radial distribution

How it can be seen, the radial distributions are practically coincident with an relative error of the order of 10^{-4} , which is evaluated as:

$$err = \frac{|f_{original} - f_{method}|}{max(f_{original})} \quad (3.2)$$

Test case 1 with noise

Since in the experiments can be present noise in the data, that can be generated for example from the detection device, e.g. CCD sensor, it is considerable to see how this method works in the noise presence.

The noise originated from the CCD sensor can be adequately described by white Gaussian noise and normally the signal-to-noise ratio (SNR) allows to describe the power of noise in a projection [20]. Therefore, such noise can be superimposed to the projection of the known radial distribution of test case 1. When applying the code to this function with noise, it can be seen if such radial distribution is recovered.

To generate the noise, it has been used the following Matlab-function which add a white Gaussian noise to signal:

$$awgn(in,snr,sigpower,s)$$

in which the vector in is the projection that must be inverted, snr is the signal-to-noise ratio per sample in dB of ICCD camera which characterizes the quality of a measurement and determines the ultimate performance of the system, the $sigpower$ is the power of in in dBW and will be posed equal to 0 and s is a random stream handle which permits to generate repeateable noise samples and will be posed equal to 2.

Assuming to have for example a $SNR = 5$, the theoretical radial distribution and the projection without and with noise can be reported in the figs. 3.5 and 3.6

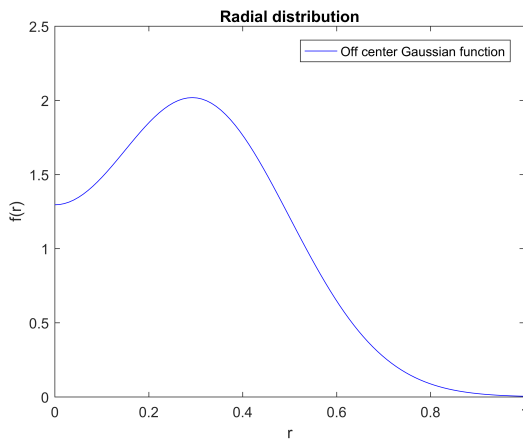


Figure 3.5: Gaussian function radial distribution

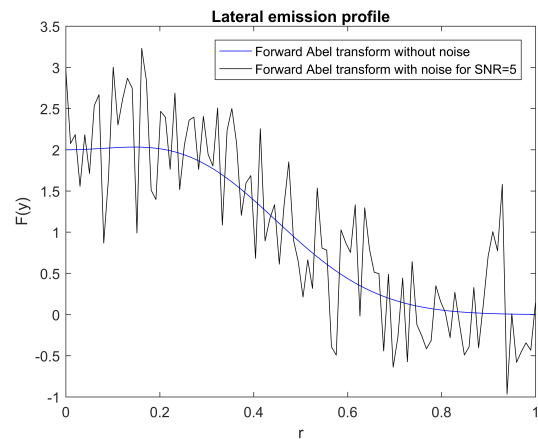


Figure 3.6: Gaussian function projection with and without noise

The results of the code application to the projection with a white Gaussian noise with an upper frequency chosen equal to 4 are represented in figs. 3.7 and 3.8

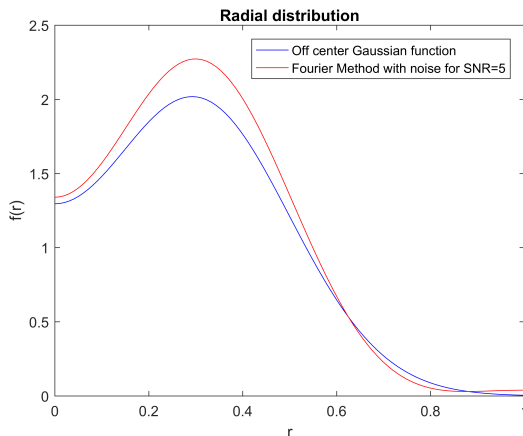


Figure 3.7: Comparison between theoretical radial and reconstrued radial distribution for $SNR=5$

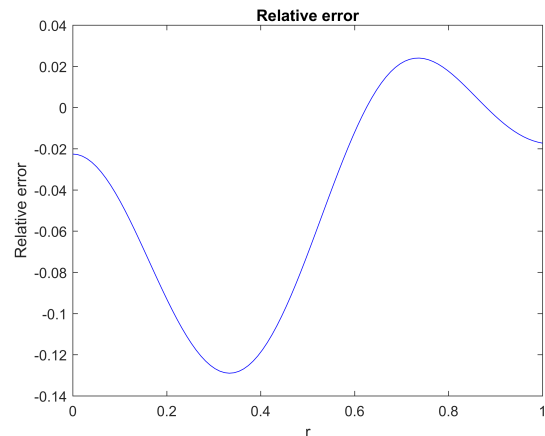


Figure 3.8: Relative error between theoretical radial and reconstrued radial distribution for $SNR=5$

Note that the theoretical radial distribution has been almost obtained, confirming that the code based on Fourier method works well also in presence of unavoidable noise. It is possible because the method is able to smooth the noise with a correct choice of upper frequency upf which allows an efficient low-pass filtering. However, note that the noise presence has reduced the quality of the reconstruction with a relative error of the order of 10^{-1} , higher than the case of test function 1 without the noise.

To see practically as what has been said, once again the Gaussian function lateral projection of test case 1 can be considered with the same white Gaussian noise, corresponding to $SNR = 5$, for different values of the upper frequency upf . The results are represented in the figs. 3.9, 3.10, 3.11 and 3.12 where note that a higher frequency translates in a better reconstruction, but it is not possible to go too far with the upf because the method low-pass filtering of the noise is lost.

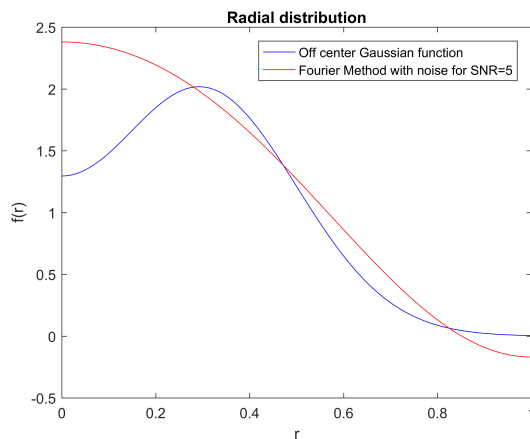


Figure 3.9: Comparison between theoretical and reconstrued radial distribution for $SNR=5$ and $upf = 2$

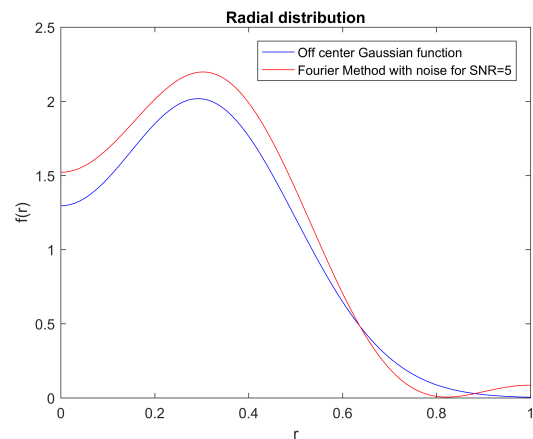


Figure 3.10: Comparison between theoretical and reconstrued radial distribution for $SNR=5$ and $upf = 3$

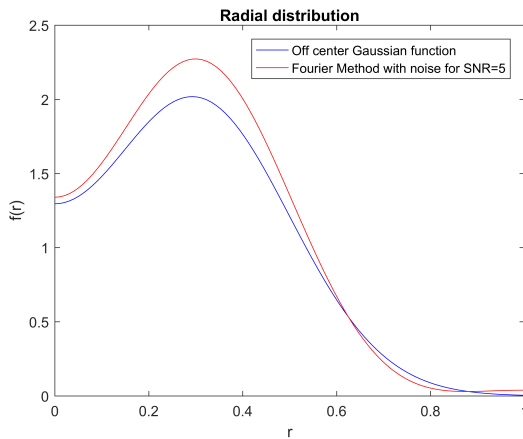


Figure 3.11: Comparison between theoretical and reconstructed radial distribution for $SNR=5$ and $upf = 4$

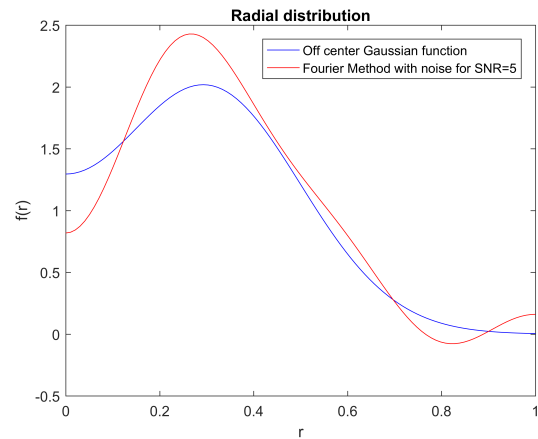


Figure 3.12: Comparison between theoretical and reconstructed radial distribution for $SNR=5$ and $upf = 5$

It is possible to see better what has been seen by the comparison between relative errors in fig. 3.13 where it decreases with increasing of upper frequency until for an $upf = 5$ the reconstruction is worse than that for an $upf = 4$. It is the reason why it was not possible to choose an $upf = 10$ as in the case without noise, selecting an $upf = 4$.

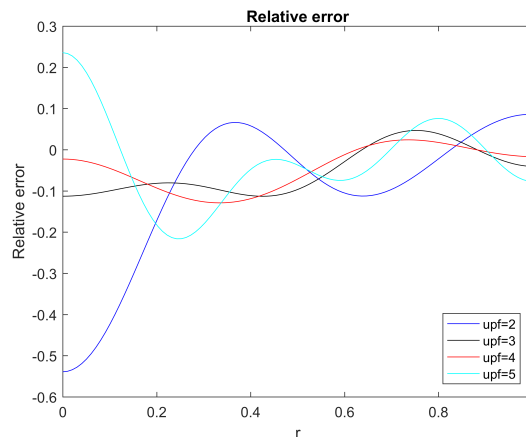


Figure 3.13: Comparison between relative errors for different upf

Furthermore, in the choice of this upper frequency it is important to note that the noise is present at the high frequencies and that the amount of present noise, e.g. the signal-to-noise ratio SNR , affects the quality of the reconstruction : an greater ratio, which it is equivalent to a lower noise at higher frequencies, allows to have a better reconstruction for the same upf .

Equally, four different white Gaussian noises, corresponding to $SNR = 5, 10, 15, 20$ can be considered superimposed to the Gaussian function lateral projection of case test 1 and these four different projection can be processed with the same upper frequency $upf = 4$. The reconstructed radial distributions for the different noises compared to the theoretical radial distribution are represented in figs. 3.14, 3.15, 3.16 and 3.17

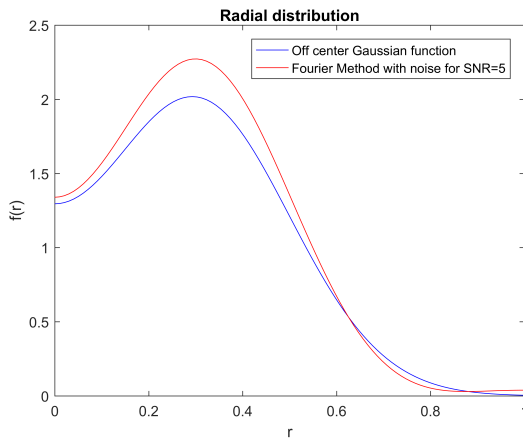


Figure 3.14: Comparison between theoretical and reconstrued radial distribution for $SNR=5$ and $upf = 4$

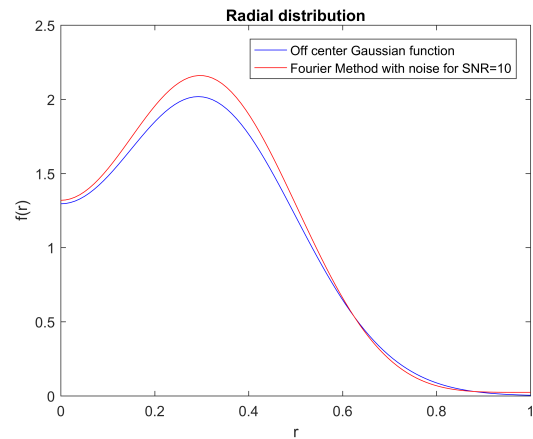


Figure 3.15: Comparison between theoretical and reconstrued radial distribution for $SNR=10$ and $upf = 4$

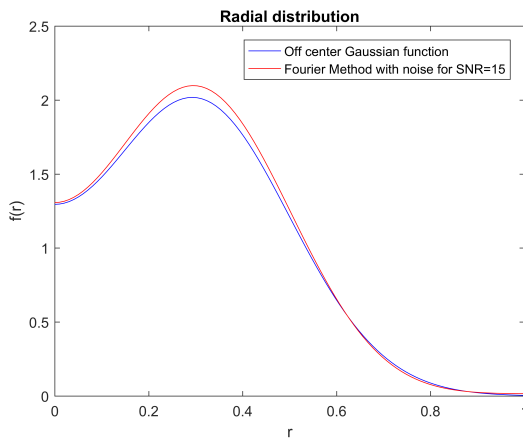


Figure 3.16: Comparison between theoretical and reconstrued radial distribution for $SNR=15$ and $upf = 4$

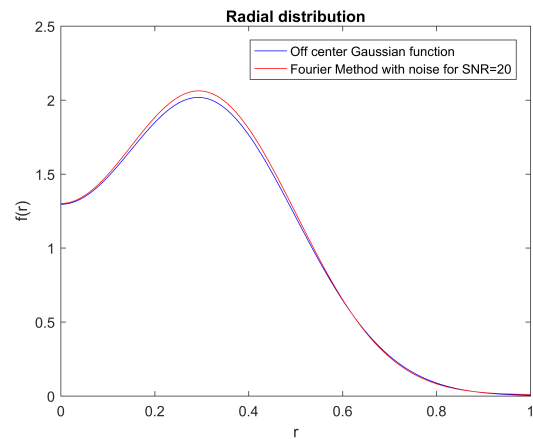


Figure 3.17: Comparison between theoretical and reconstrued radial distribution for $SNR=20$ and $upf = 4$

Note that, as anticipated, the reconstruction is better for the same *upper frequency* when the noise decreases as it is possible to see by the comparison between relative errors in fig. 3.18

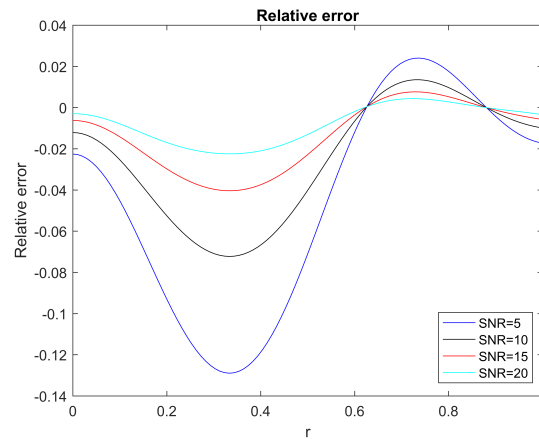


Figure 3.18: Comparison between relative errors for different SNR

Test case 2

As second test case referring to H. Fulge et al. [8] a single cubic function has been chosen expressed as :

$$f(r) = ar^3 + br^2 + cr + d \quad (3.3)$$

in which r is a vector of equidistant values taken from 0 to 1, while the parameters a , b , c , d are chosen from the necessary boundary conditions:

$$f(0) = 3$$

$$f(1) = 0$$

$$f'(0) = 0$$

$$f'(1) = 0$$

The function of the equation 3.3 is forward Abel transformable analytically to:

$$F(y) = \frac{1}{12}(\sqrt{(r^2 - y^2)}(24d + 12cr + 8br^2 + 6ar^3 + 16by^2 + 9ary^2) + 3(4cy^2 + 3ay^4)\log(r + \sqrt{(r^2 - y^2)})) \Big|_{r=y}^{r=1} \quad (3.4)$$

The original radial distribution and its forward Abel transformed are shown in the figs. 3.19 and 3.20

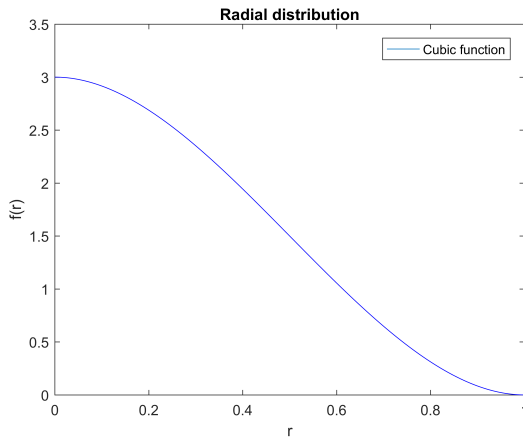


Figure 3.19: Cubic function radial distribution

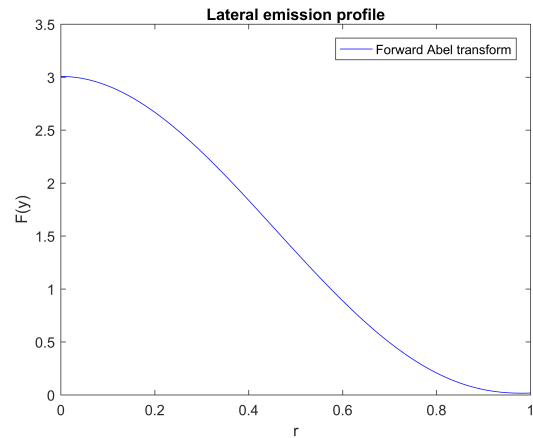


Figure 3.20: Forward Abel of Cubic function

Once again, it is possible to apply the inverse Abel transform to the lateral emission profile to see the differences between the original radial distribution and the reconstrued radial distribution. The results obtained with an $upf = 10$ are shown in figs. 3.21 and 3.22

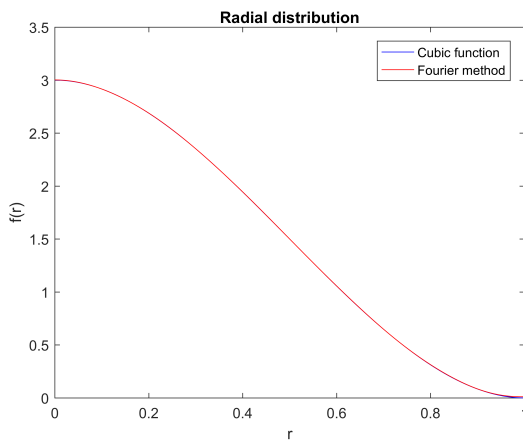


Figure 3.21: Cubic function: comparison between therotical and reconstrued radial distribution

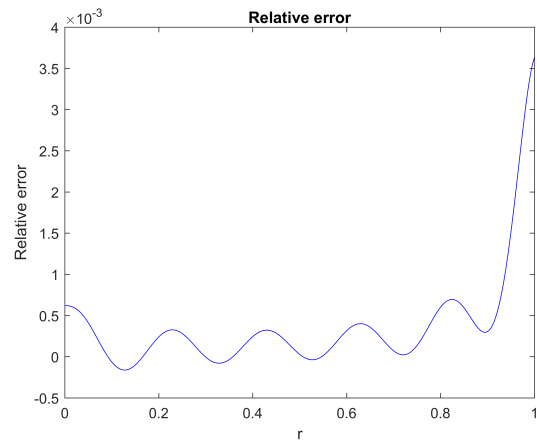


Figure 3.22: Cubic function: relative error between theretical and reconstrued radial distribution

Also in this case, the Fourier method give good results, with the radial distributions substantially coincident with an error of the order of 10^{-3} .

Test case 2 with noise

It can be considered also the presence of a noise described by a white Gaussian noise superimposed to the lateral projection profile of test case 2.

The theoretical radial distribution and the relative lateral projection with and without the noise are represented in the figs. 3.23 and 3.24

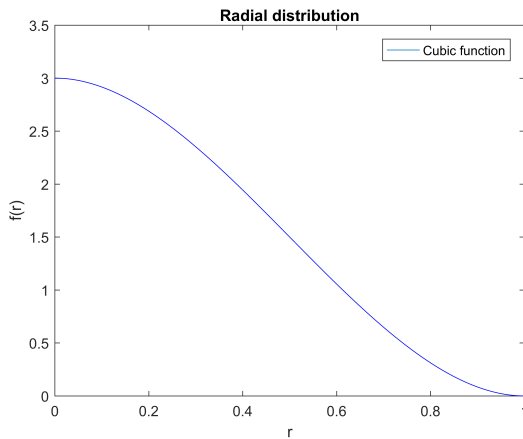


Figure 3.23: Cubic function radial distribution

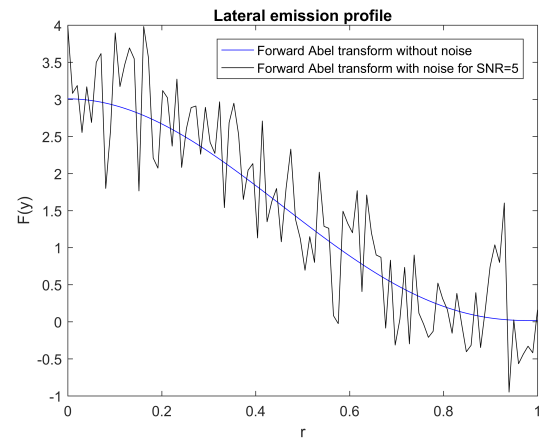


Figure 3.24: Cubic function projection with and without a white Gaussian noise

The obtained results applying the code for an $upf = 4$ to the projection with a superimposed white Gaussian noise for SNR=5 are reported in figs. 3.25 and 3.26

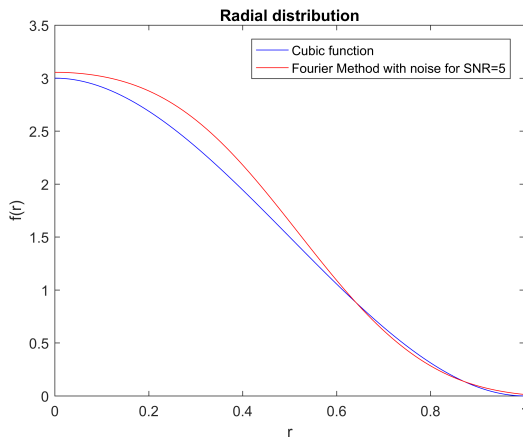


Figure 3.25: Cubic function: comparison between theoretical and reconstructed radial distribution

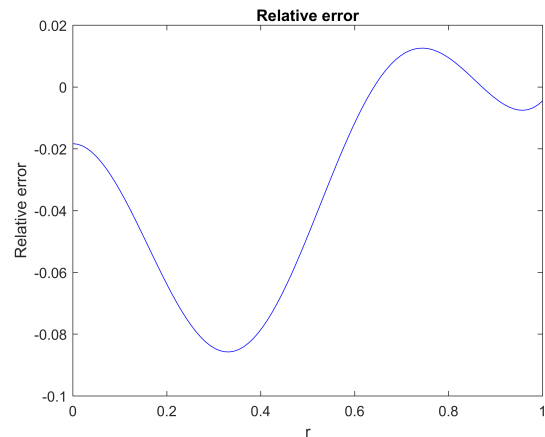


Figure 3.26: Cubic function: relative error between theoretical and reconstructed radial distribution

Note that also in this case, although the noise presence, the code returns almost the theoretical radial distribution. However, once again the noise affects the reconstruction with an error of the order of 10^{-1} that results to be higher than the case of test function

2 without noise.

It is possible also in this case evaluate what upper frequency upf allows to get the best reconstruction with the minimum relative error for fixed signal to noise ratio.

Considering still an signal to noise ratio $SNR = 5$, it has be tried to recover the radial distribution with four different upper frequencies $upf = 2,3,4,5$. The results are reported in figs. 3.27, 3.28, 3.29, 3.30

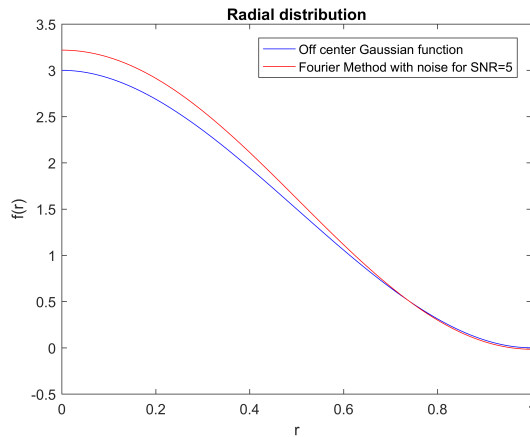


Figure 3.27: Cubic function: comparison between theoretical and reconstrued radial distribution for $SNR=5$ and $upf=2$

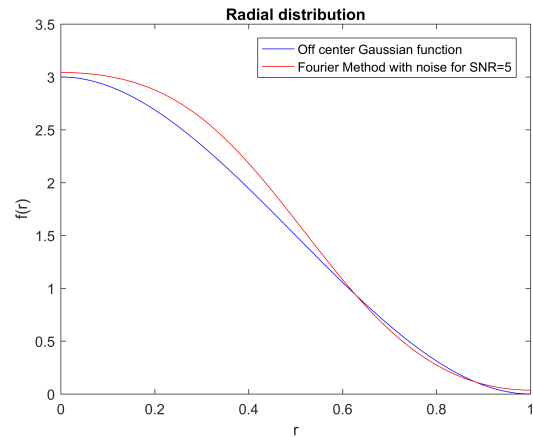


Figure 3.28: Cubic function: comparison between theoretical and reconstrued radial distribution for $SNR=5$ and $upf=3$

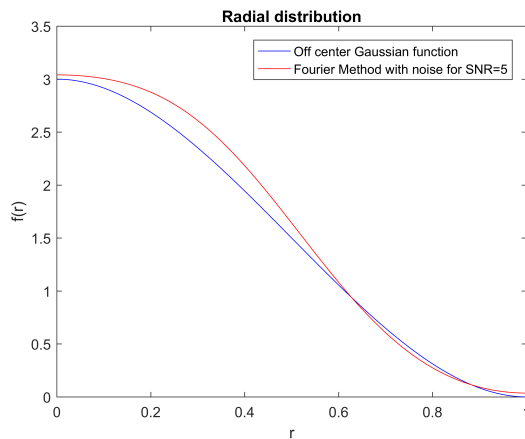


Figure 3.29: Cubic function: comparison between theoretical and reconstrued radial distribution for $SNR=5$ and $upf=4$

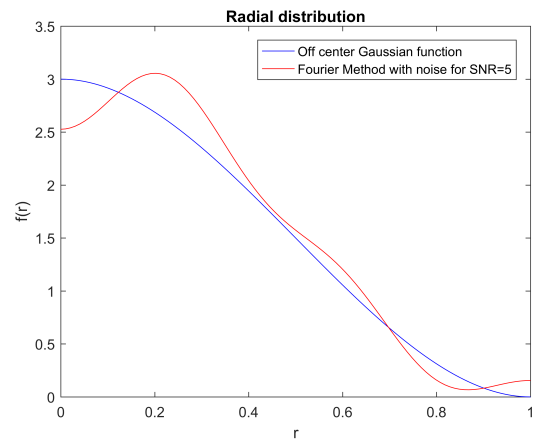


Figure 3.30: Cubic function: comparison between theoretical and reconstrued radial distribution for $SNR=5$ and $upf=5$

Once again, it can be seen that an increase in upper frequency upf allows to obtain a better reconstruction, but go too far may result in a loss of the low-pass filter properties. What has been said can be seen considering the relative error to change of the upper

frequency in fig. 3.31 , where an $upf = 5$ give results worse than $upf = 4$. Furthermore, it can be noted that the reconstructions with $upf = 3$ and $upf = 4$ are practically superimposed with results slightly better at the centre for this last frequency. So, it confirms that a right choice can be to consider an upper frequency $upf = 4$.

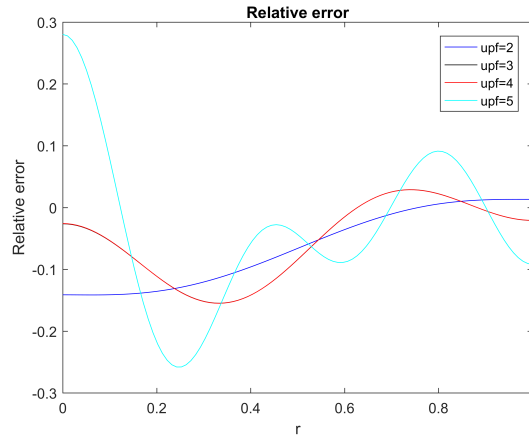


Figure 3.31: Comparison between relative error for different upf

Test case 3

The third test function considered with the known Abel inversion lateral distribution is taken from [18]:

$$f(r) = 1 - 3r^2 + 2r^3 \quad 0 \leq r \leq 1 \quad (3.5)$$

$$F(y) = \sqrt{(1 - y^2)}(1 - 2.5y^2) + 1.5y^4 \ln\left(\frac{1 + \sqrt{1 - y^2}}{y}\right) \quad 0 \leq y \leq 1 \quad (3.6)$$

In reality, since in some measured profiles there is the presence of zero emissivity in the centre, it can be useful to consider a test function with such characteristic. So a new test function for the radial emissivity is obtained subtracting the test function 3 with 100 data points from the same function evaluated with 200 data points. Furthermore, it is possible to apply the same procedure to the lateral distribution. It will be the Abel direct of the new radial emissivity because the Abel transform of the sum of two profiles is equal to the sum of the Abel transform of two profiles [21].

In figs. 3.32, 3.33, 3.34, 3.35 are represented the test function, its theoretical lateral distribution and the results of the Abel inversion code obtained with $upf=10$.

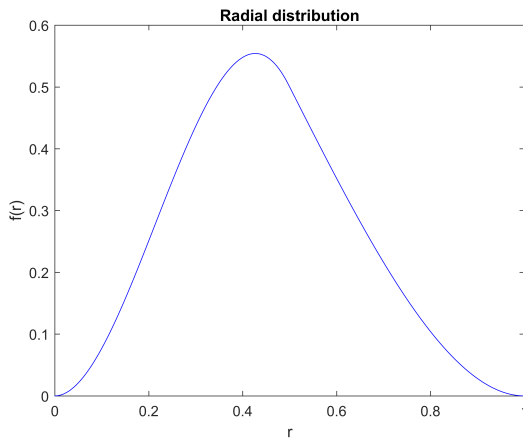


Figure 3.32: New test function radial distribution

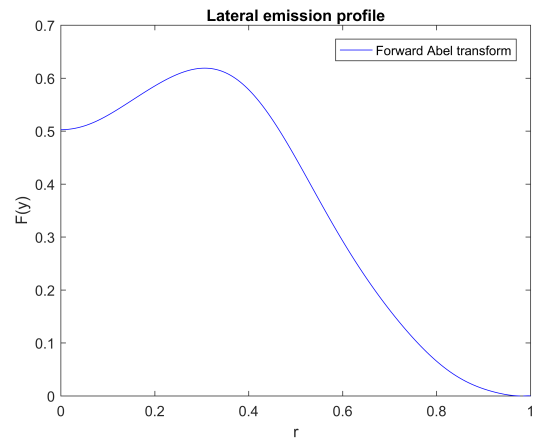


Figure 3.33: Lateral projection of test function

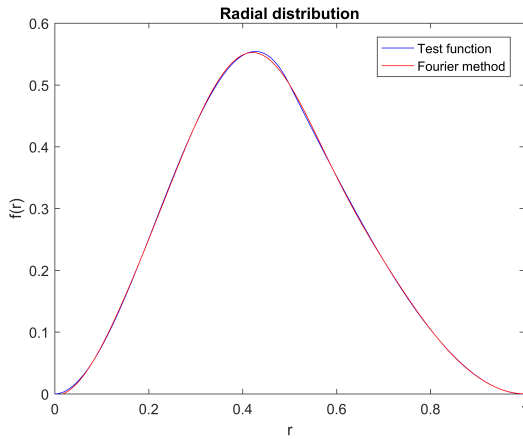


Figure 3.34: New test function: comparison between theoretical and reconstructed radial distribution

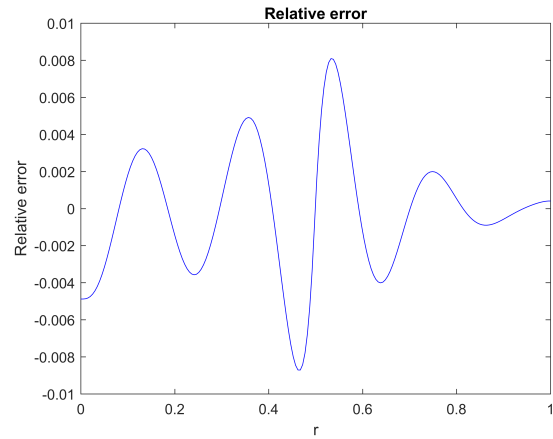


Figure 3.35: New test function: relative error between theoretical and reconstructed radial distribution

How is it possible to see, the theoretical radial profile and the profile obtained from the inversion Abel algorithm are almost identical with a relative error of the order of 10^{-3} .

Test case 3 with noise

Again, the noise in the experimental measurements can be simulated in order to study the impact on the measurement also for this profile.

A white Gaussian noise can be considered superimposed to the lateral profile and the Abel inversion is applied to the resultant profile with noise.

An SNR=20 has been chosen in this case and the reconstruction has been done with an upper frequency $upf = 4$. The results are represented in figs. 3.36, 3.37, 3.38, 3.39, where it can be seen that the theoretical radial distribution is recovered with a relative error of order of 10^{-1} . Once again note that this error is higher than the case of function 3 without noise.

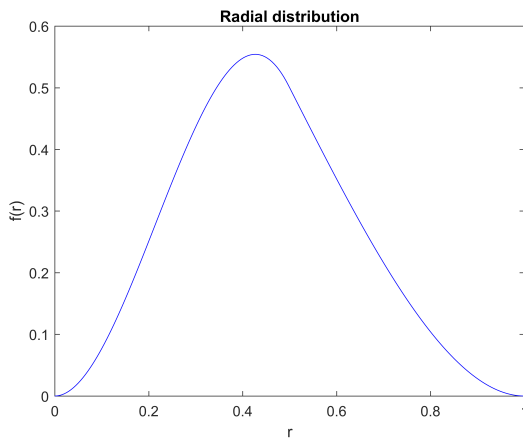


Figure 3.36: New test function radial distribution

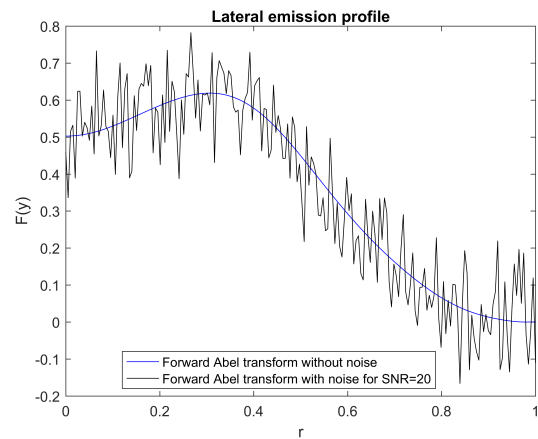


Figure 3.37: Lateral projection with and without a white Gaussian noise

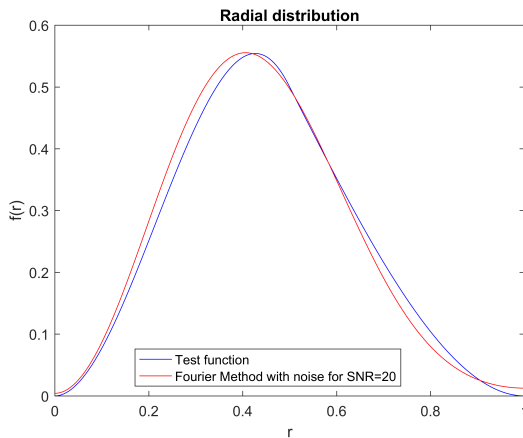


Figure 3.38: New test function: comparison between theoretical and reconstructed radial distribution for SNR=20 and $upf=4$

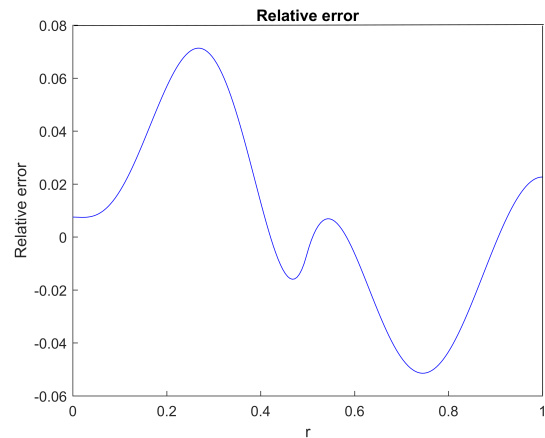


Figure 3.39: New test function: relative error between theoretical and reconstructed radial distribution for SNR=20 and $upf=4$

Note that the noise presence involves that to obtain a good reconstruction the expansion number results to be lower than the case without noise to have the correct low-pass filter.

Furthermore, for this function and for a $\text{SNR}=20$, an upper frequency upf is once again chosen equal to 4 because it has been seen that the noise at high frequencies does not look to change with the SNR, that affects only the amount of the noise.

In fact it is possible to report the different reconstruction profiles obtained by means of different upf with the relative errors in figs. 3.40, 3.41, 3.42, 3.43, 3.44 and to see that the best results are still obtained with such upf .

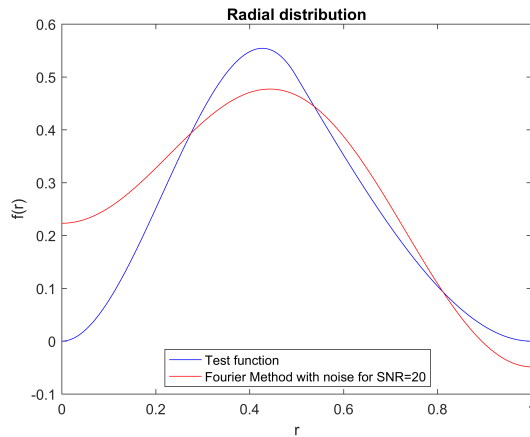


Figure 3.40: Comparison between theoretical and reconstructed radial distribution for $\text{SNR}=20$ and $upf=2$

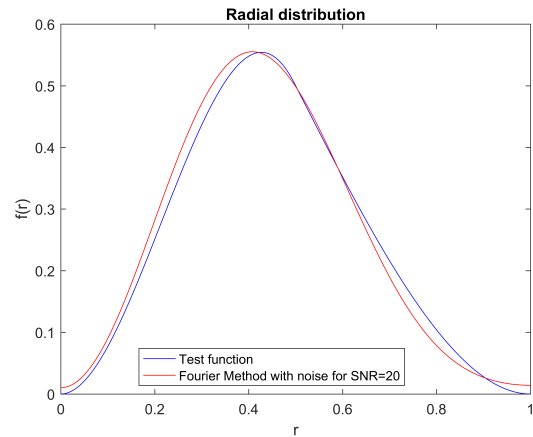


Figure 3.41: Comparison between theoretical and reconstructed radial distribution for $\text{SNR}=20$ and $upf=3$

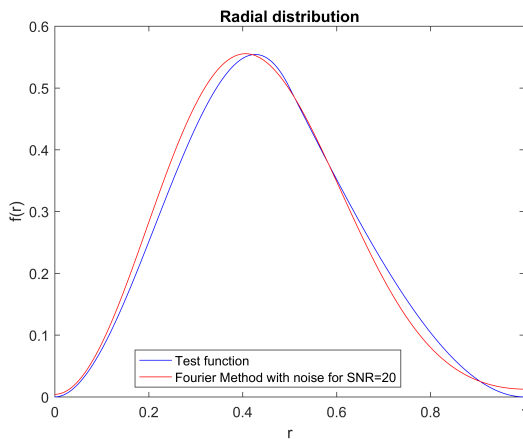


Figure 3.42: Comparison between theoretical and reconstructed radial distribution for $\text{SNR}=20$ and $upf=4$

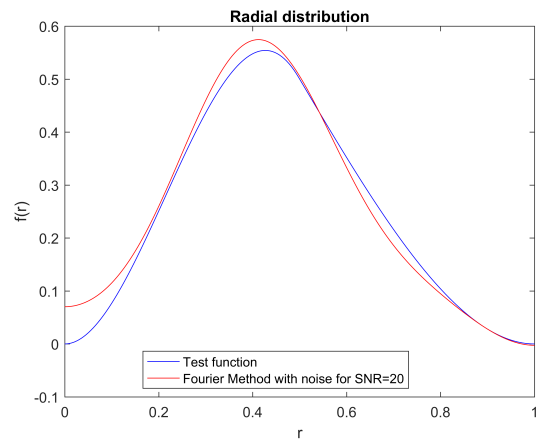


Figure 3.43: Comparison between theoretical and reconstructed radial distribution for $\text{SNR}=20$ and $upf=5$

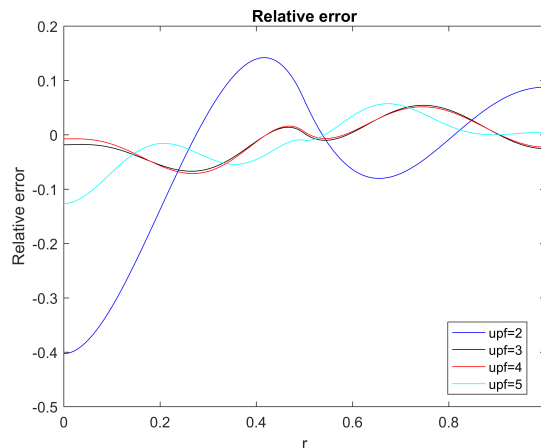


Figure 3.44: Comparison between relative error for different upf

3.2.2 2D Case

Once tested the code with the known radial distribution functions taken from the literature, some 2D radial distribution or images can be considered and the code can be applied to them to verify if it works properly also in this case.

However, the literature does not provide the know radial distribution functions in 2D case, so in an alternative way it has been chosen to apply the code to the recorded images that was recorded with ICCD camera.

Since the radial distribution $f(r,z)$ of these images are not known because it is what must be obtained, to check the code the images data, e.g. the projection, are first inverted and after numerically forward Abel transformed, so the images and the calculated projections can be compared.

Considering for example the experimental test case Methane pressure 20 bar ROF=2.2, 2.6, 3.0, 3.4 represented in fig. 3.45, in which the upper half corresponds to the original flame image and the down half corresponds to the image generated with the code, it has to be pointed out that the pictures agree well.

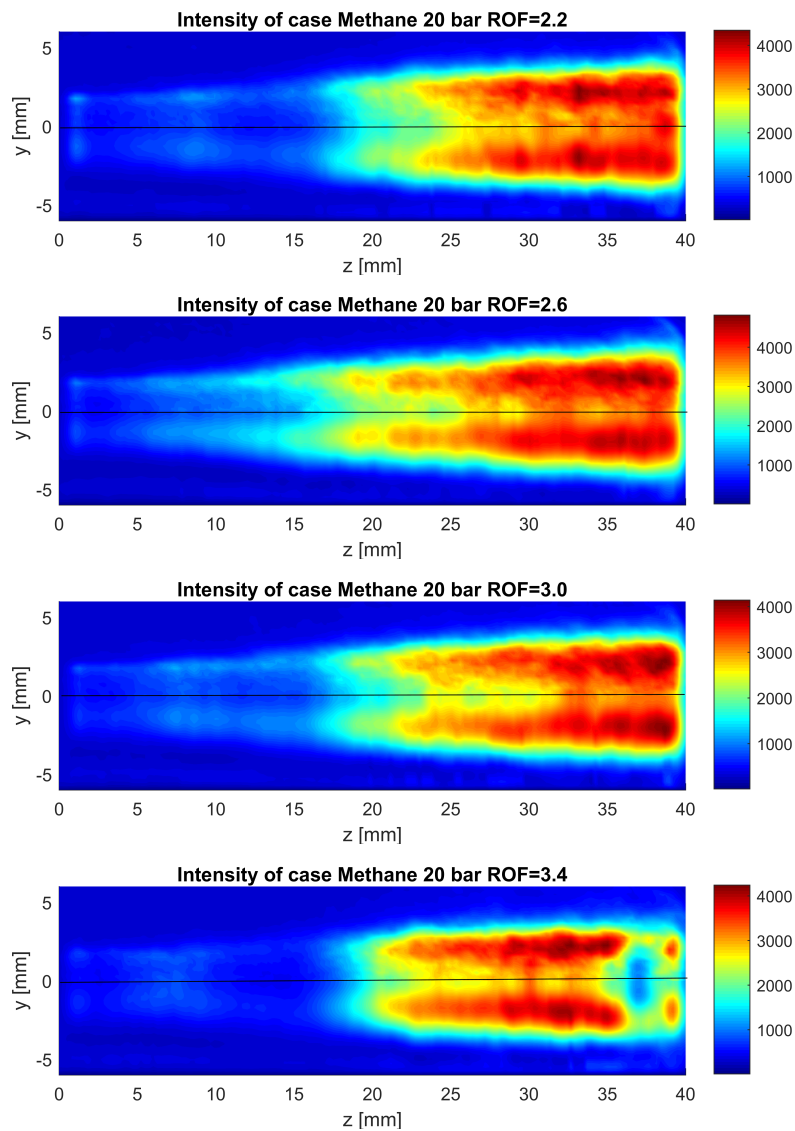


Figure 3.45: Recorded and recovered intensity images for Methane pressure 20 bar ROF = 2.2, 2.6, 3.0, 3.4

As a better confirmation of the goodness of the results for each test a specific column of both images, e.g. a specific radial profile for a fixed axial position, can be chosen to do a comparison between the intensities. Considering for example a station along the axial direction $z = 30 \text{ mm}$, the radial profiles are represented in fig. 3.46 where it is possible to see that the intensity shape is well recovered.

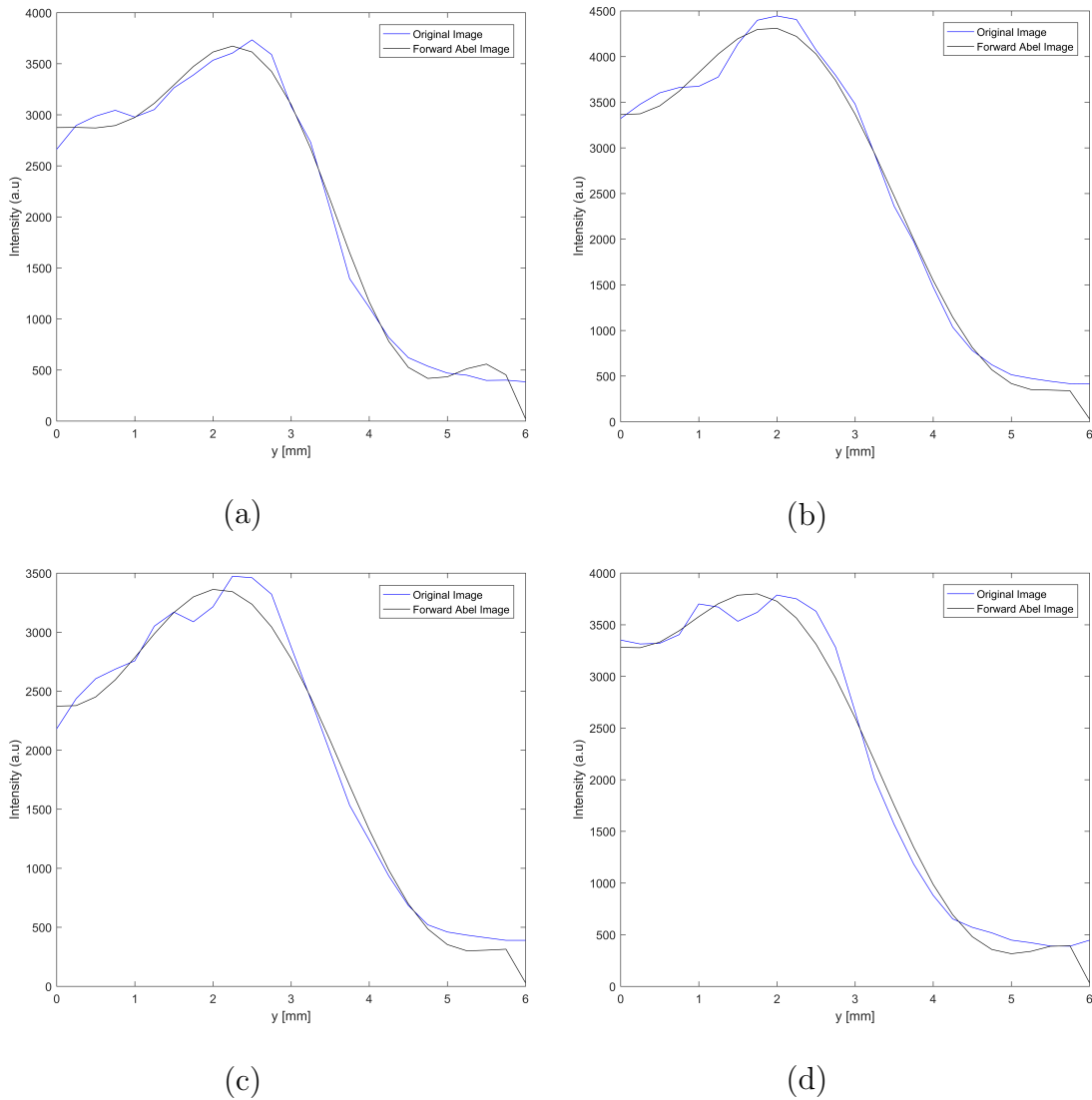


Figure 3.46: Comparison between the image and calculated intensity values for the axial position $z=30$ mm for ROF (a) 2.2, (b) 2.6, (c) 3.0, (d) 3.4

The unique substantial differences are visible at the outer boundary, due to the fact that the reflection of the window and not application of the shading correction the intensity values in this position are not equal to zero. Because the Abel transform is really sensitive to these problems, it returns wrong emission values.

Chapter 4

Experimental data

The test campaign concerned the study of the combustion process of the propellents combination GOX/GCH_4 and GOX/GH_2 . A certain number of test were conducted with these propellents at different test conditions in terms of combustion chamber pressure P_{cc} and mixture ratio ROF represented in table 4.1

Propellent	CH_4		H_2	
P_{cc}	10 bar	20 bar	10 bar	20 bar
ROF	2.2	2.2	4.4	4.4
ROF	2.6	2.6	5.2	5.2
ROF	3.0	3.0	6.0	6.0
ROF	3.4	3.4	6.8	/

Table 4.1: Load points

Note that for the test case 20 bar ROF 6.8 was not carried out for Hydrogen because of high temperatures which could have lead to combustion chamber damages.

In order to have the flame stable phase only the instantaneous images of the three seconds of burning time have been considered for each test, neglecting those corresponding to the start-up and shut-down. The images for every test are then averaging, obtaining an average image, to smooth the noise and the flame fluctuations.

The used experimental images refer to those published in the P. Difficile [2] and G. Laera's [3] Masterthesis, to whose reference is made for further details.

Because of the problems in the experimental post-processing phase for the application of shading correction, it was chosen to use the images without this correction.

Furthermore, to satisfy the Abel transform assumption of axisimmetry, these images are processed and an axisimmetric image is obtained averaging the values at same distance

from the flame center of the upper and down half of average image.

An overall flame image can be obtained mirroring the average image about the axis of simmetry.

The images used fot the application of inverse Abel transform are reported in fig. 4.1, 4.2, 4.3, 4.4

Hydrogen

- $P_{cc} = 10$ bar

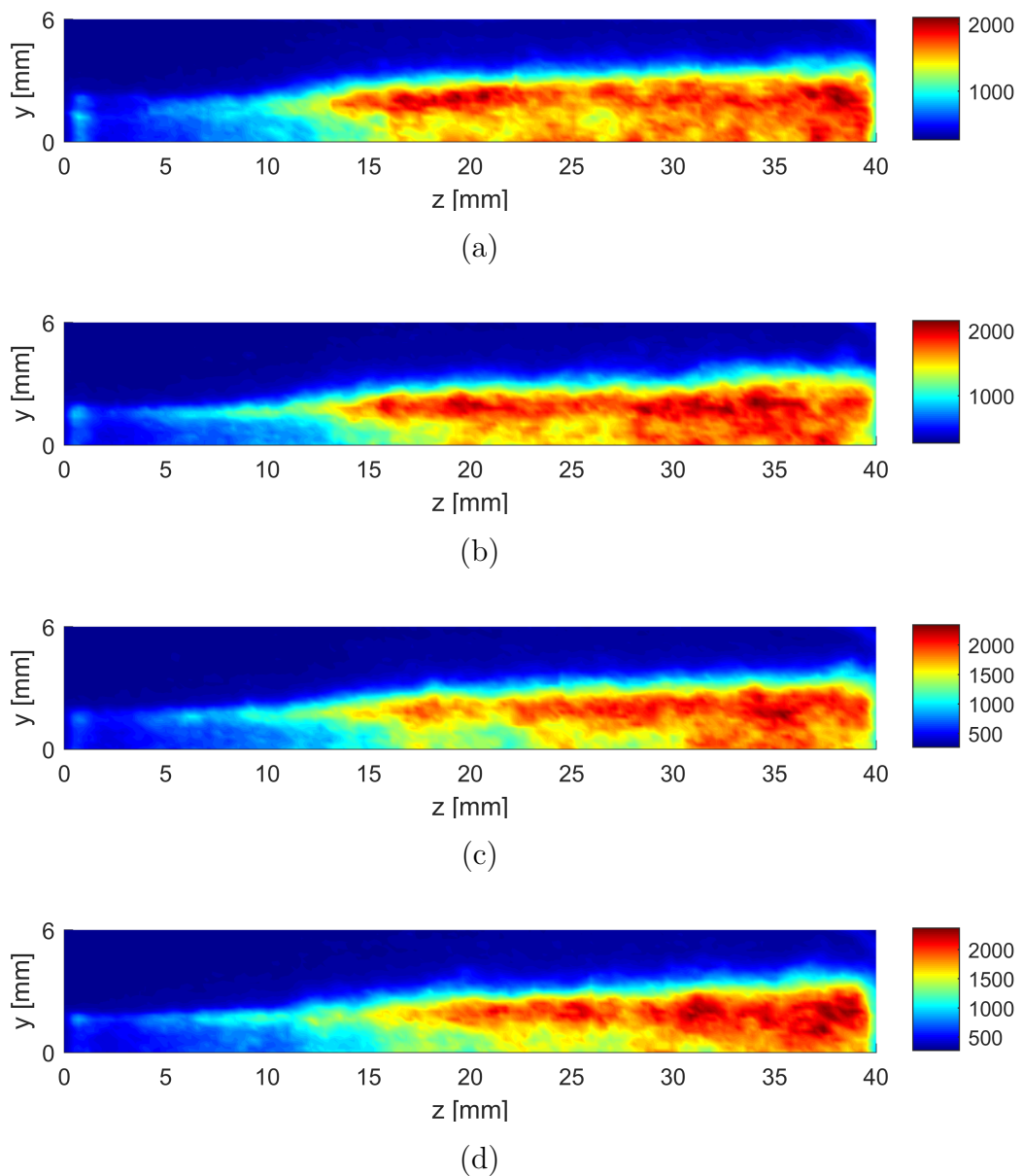
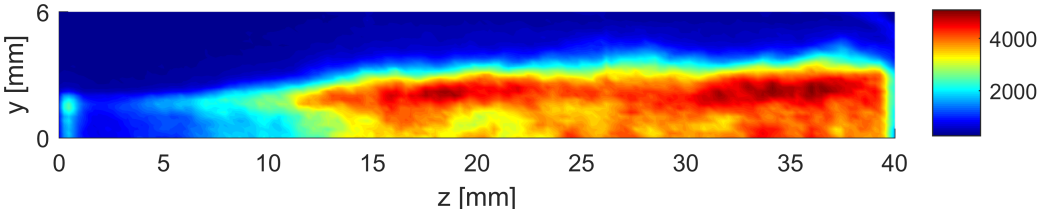
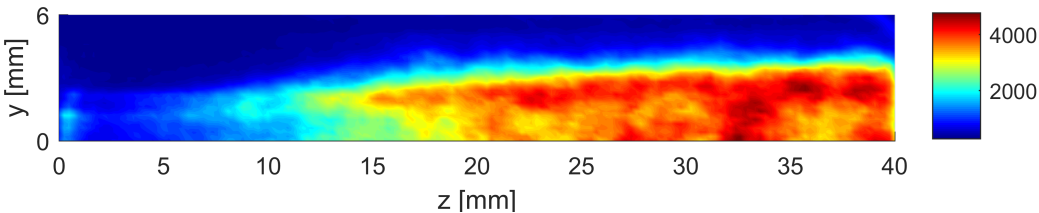


Figure 4.1: Hydrogen ROF (a) 4.4 (b) 5.2 (c) 6.0 (d) 6.8

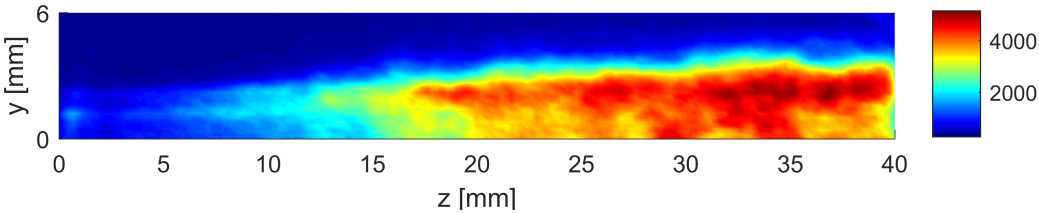
- $P_{cc} = 20$ bar



(a)



(b)



(c)

Figure 4.2: Hydrogen ROF (a) 4.4 (b) 5.2 (c) 6.0

Methane

- $P_{cc} = 10$ bar

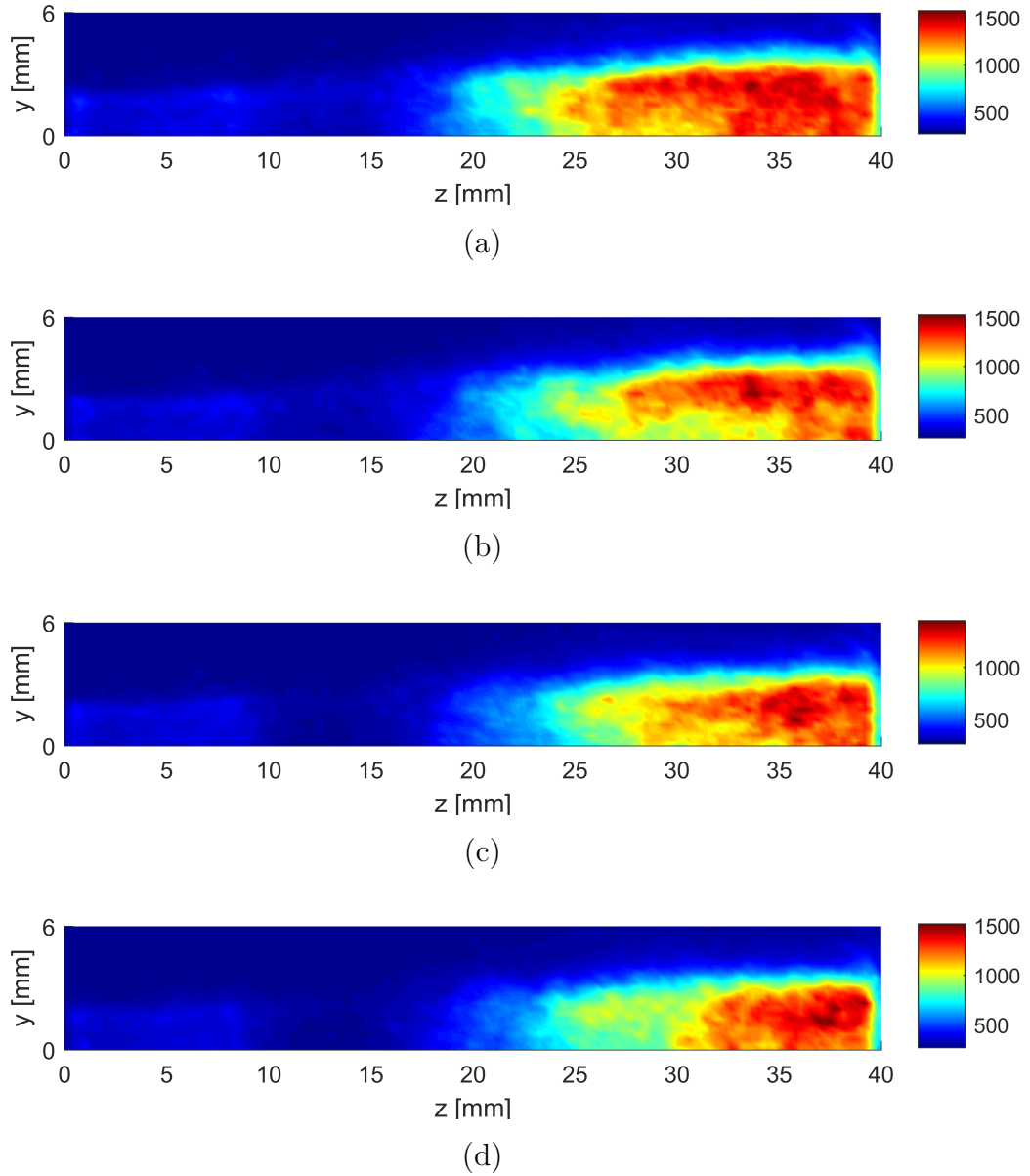
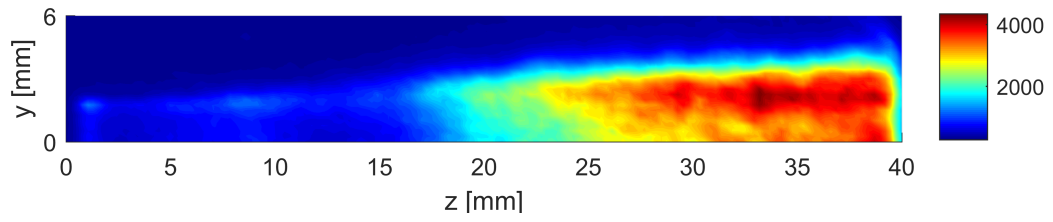
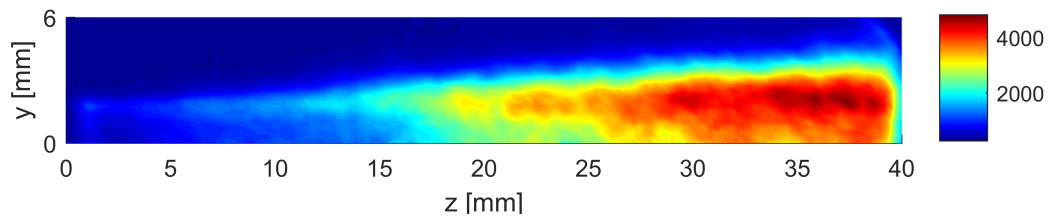


Figure 4.3: Methane ROF (a) 2.2 (b) 2.6 (c) 3.0 (d) 3.4

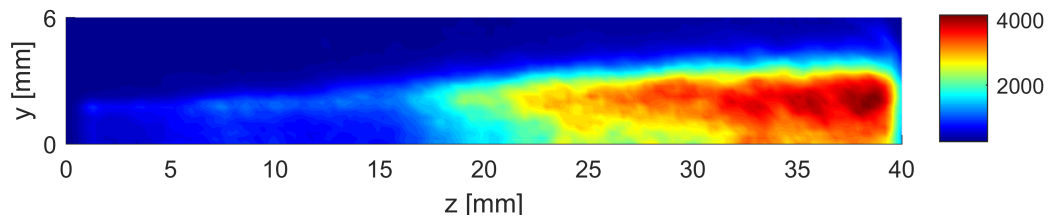
- $P_{cc} = 20$ bar



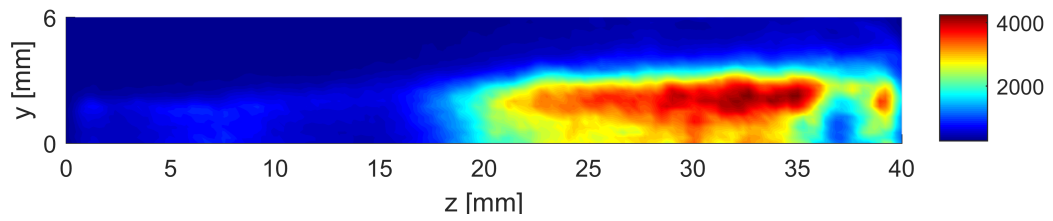
(a)



(b)



(c)



(d)

Figure 4.4: Methane ROF (a) 2.2 (b) 2.6 (c) 3.0 (d) 3.4

Chapter 5

Results

Once identified the images that have to be used, it is possible to apply the inverse Abel transform to the experimental data to recover the local emission radial distribution. Since it has been seen by the considered test function that the best value to smooth the noise at high frequencies is an $upf = 4$, corresponding to a number of cosine for the expansion equal to 5, the results are obtained with this upper frequency. Note that the number of expansion cosine affects both the filtering effects and computation time.

Because of an incorrect determination of the center, the asymmetry and the noise filtering there is the presence of negative emission values as results of the algorithm application. Such not physical values are then set to zero.

Futhermore, to make the flame shape and anchoring more visible the flame shape and anchoring, both for GOX/GH_2 and for GOX/GCH_4 the emission intensities are normalized to the maximum emission detected for all ROF cases.

Such maximum values are reported in table 5.1

	GOX/GH_2	GOX/GCH_4
$P_{cc} = 10 \text{ bar}$	361.8503	218.3529
$P_{cc} = 20 \text{ bar}$	787.9613	679.0374

Table 5.1: Maximum Emission Intensity to change of pressure and propellant pair

5.1 Hydrogen

The reconstrued radial distributions for the GOX/GH_2 for pressure P_{cc} equal to 10 and 20 bar to ROF variation are represented in figs. 5.1 and 5.2

- $P_{cc} = 10$ bar

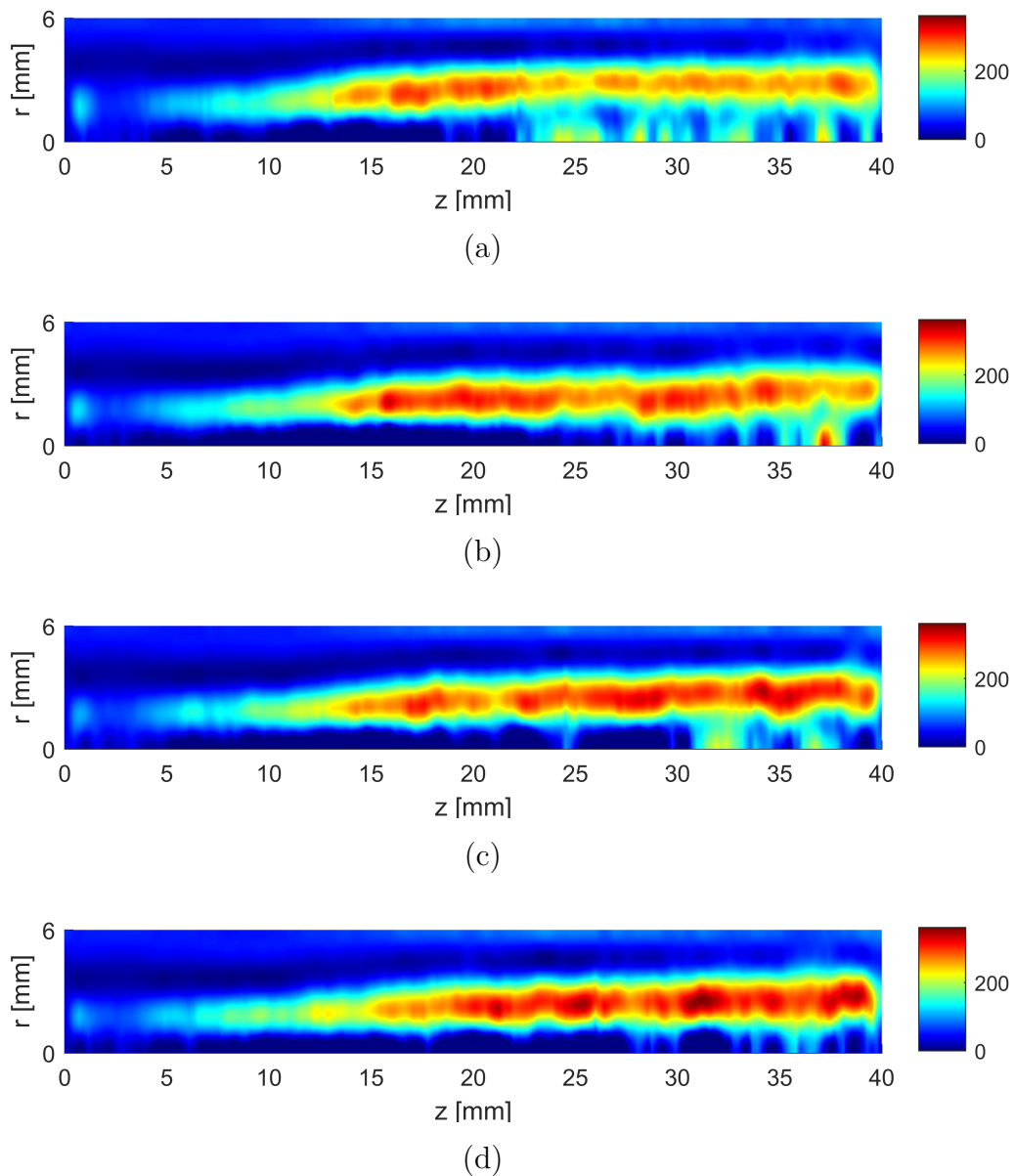


Figure 5.1: Test Hydrogen 10 bar (a) $ROF=4.4$ (b) 5.2 (c) 6.0 (d) 6.8

- $P_{cc} = 20$ bar

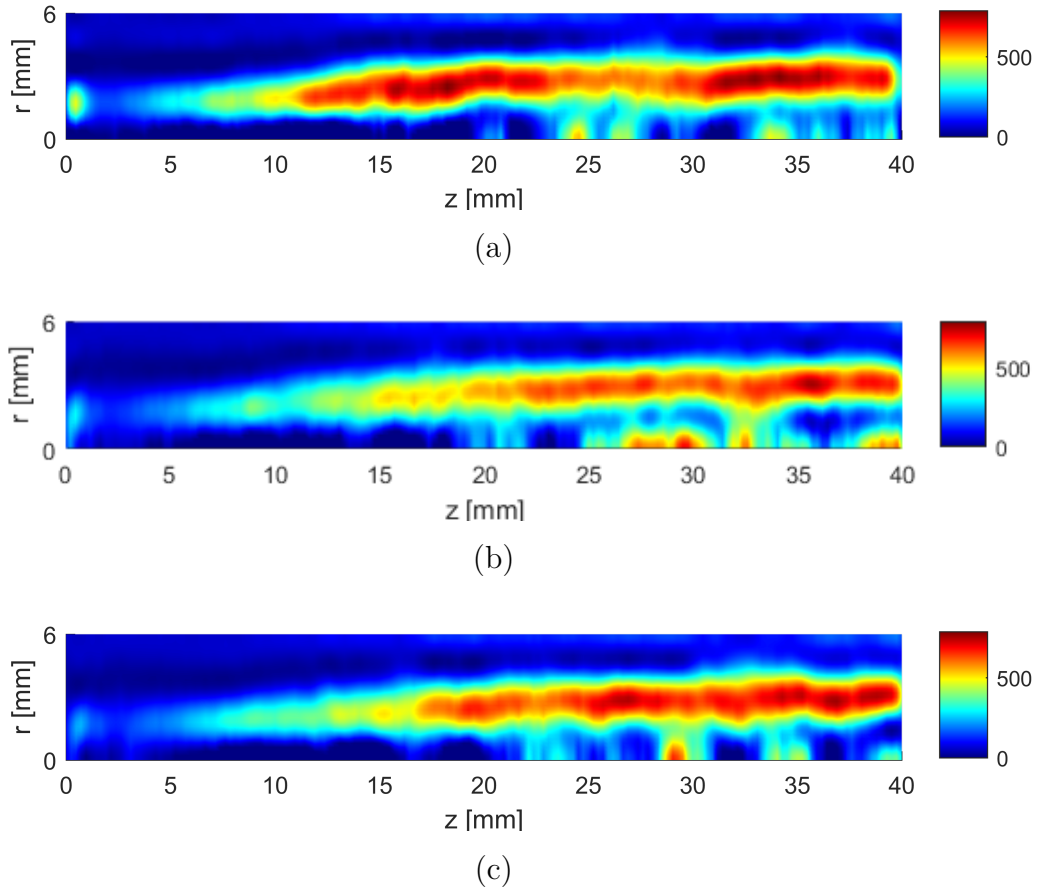


Figure 5.2: Test Hydrogen 20 bar (a) ROF=4.4 (b) 5.2 (c) 6.0

Note that in all cases the flame is attached and incloses the oxygen jet and shows the familiar crescent shape, with little emission at the flame base and higher emission at the end of the image.

This is in agreement with Fiala that the mostly emission is located at the tip of the flame, not visible in this experiment [5]. The flame follows the oxidizer jet near the injector in the first part and after an axial distance of about 3-4 times the GOX inlet internal diameter d_i , the flame slightly expands radially and diverges towards the combustion chamber walls. This characteristic flame expansion can be explained by the decrease of shear forces between the flows at a certain distance from the injector face, and is in agreement with Lux et al. [22].

This expansion seems to be insensitive to ROF variation, according with Winter et al. [1], but the OH^* is a function of it, as well as pressure.

From a preliminary study the results in terms of flame shape and anchoring seem to be

correct, presenting the typical development found in the GOX/H_2 flames and reported in literature.

Nevertheless, to prove the correctness of the reconstruction it is necessary a comparison between the different results to the pressure P_{cc} and ROF variation, checking if they are according to the results of the literature and the previous studies about these propellant combination.

What has been said includes the identification of parameters which affect the combustion process in the area of interest and discussion about the their effect.

It has already been demonstrated that the parameters which influence the near injection in a coaxial injector are the reduced pressure P_r , defined by the ratio between the combustion chamber pressure P_{cc} and the thermodynamic critical pressure of oxygen $P_{c,O_2} = 50,43 \text{ bar}$, the mixture ratio ROF , the velocity ratio VR and the momentum flux ratio J [23]

$$P_r = \frac{P_{cc}}{P_{c,O_2}}$$

$$ROF = \frac{\dot{m}_{GOX}}{\dot{m}_g}$$

$$VR = \frac{v_g}{v_{GOX}}$$

$$J = \frac{(\rho v^2)_g}{(\rho v^2)_{GOX}}$$

These parameters are linked, so a variation of pressure or ROF , that are the operating conditions changed in the test campaign, involves a variation in the other parameters.

In order to understand the their effect and to compare the different cases to provide an explanation of the results, it is necessary to normalize the deconvoluted emission images obtained from the Inverse Abel transform with respect to the maximum emission intensity obtained in all test cases carried out with the corresponding propellant pair.

For the GOX/GH_2 , the maximum emission value with which the emission radial distributions are normalized has been detected for pressure 20 bar and $ROF=4.4$, and is equal to the value for these operating conditions reported in table 5.1

With such normalized distribution, a first important consideration can be done about the pressure effect on the emission.

In fact, considering for example the normalized emission radial distribution for the test cases with $ROF = 4.4$ and pressures 10 bar and 20 bar reported in fig. 5.3 can be seen that a pressure increase translates into an higher emission. This effect occurs for all cases of ROF variation.

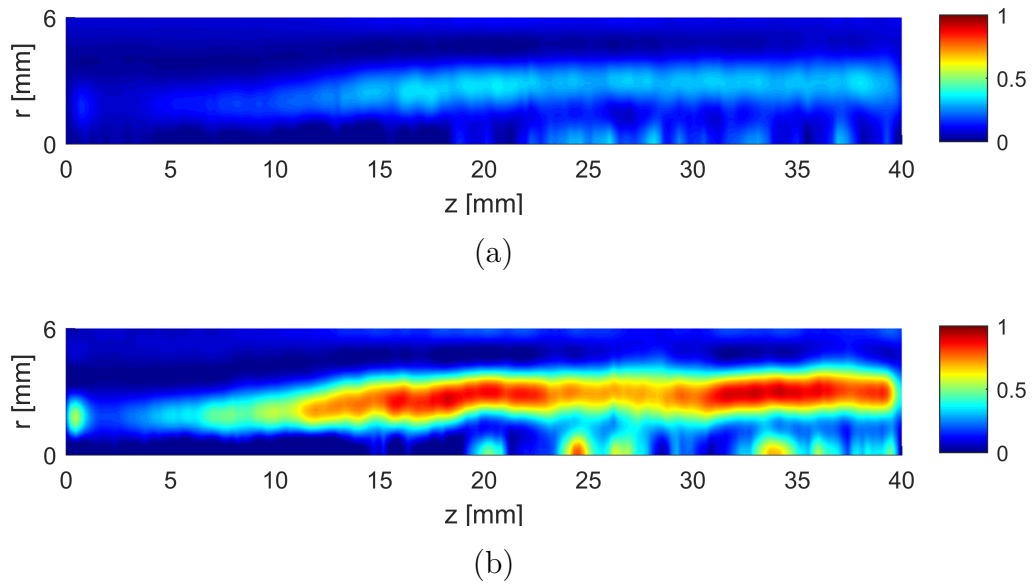


Figure 5.3: Hydrogen: $ROF=4.4$ (a) $P_{cc}=10$ bar, (b) $P_{cc}=20$ bar

To better compare, one can consider for the same test cases the development of the emission along the axial direction for the fixed distance $r = 3$ mm from the flame center [fig. 5.4]

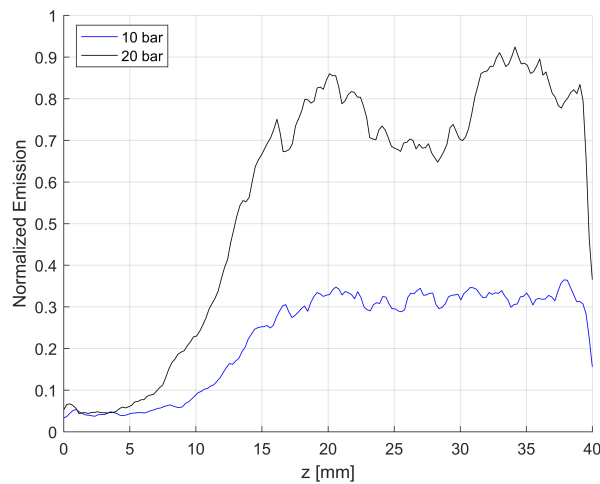


Figure 5.4: Hydrogen : normalized emission development for $ROF = 4.4$ and $P_{cc} = 10$ bar/ 20 bar along the axial direction for $r = 3$ mm

This results are in agreement with the studies of Fiala [5] in which has been shown that for the oxygen/hydrogen flames the overall integrated OH^* radiance shows to have an approximately linear increase up to a pressure of 17 bar, remaining then constant up to 30 bar.

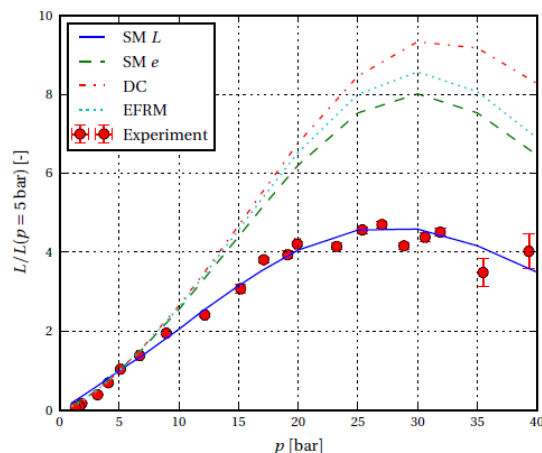


Figure 5.5: Total OH^* radiance to change of pressure [5]

The reason for this behavior can be found mainly in the fact that, at almost constant temperature, the radiation is directly proportional to the overall OH concentration. This concentration is equal to the flame thickness multiplied by the density of OH, which is directly proportional to the pressure [5].

Also, according to Fiala, the flame thickness decreases only slightly up to 17 bar, so the behavior of the overall radiation at low pressures is approximately linear.

Furthermore, at low pressure the OH^* radiation increases further due to the increase in temperature with the pressure, which has an exponential impact on the radiation [24].

About the ROF effect it is possible to consider the OH^* emission radial distribution for pressure 20 bar and different $ROF = 4.4, 5.2, 6.0$ reported in fig. 5.6. The flame results have a similar development for a ROF variation also for a combustion chamber pressure equal to 10 bar.

Note that up to a certain distance from the GOX injection the emission for the case $ROF=4.4$ is higher than that for the case $ROF = 6.0$, although the latter is closer to the stoichiometric value, equal to 8.

What has been said can be seen better taking the development of the emission along the axial direction z for a fixed distance from the flame center $r = 3 \text{ mm}$ for the $ROF = 4.4$ and $ROF = 6.0$ reported in fig. 5.7

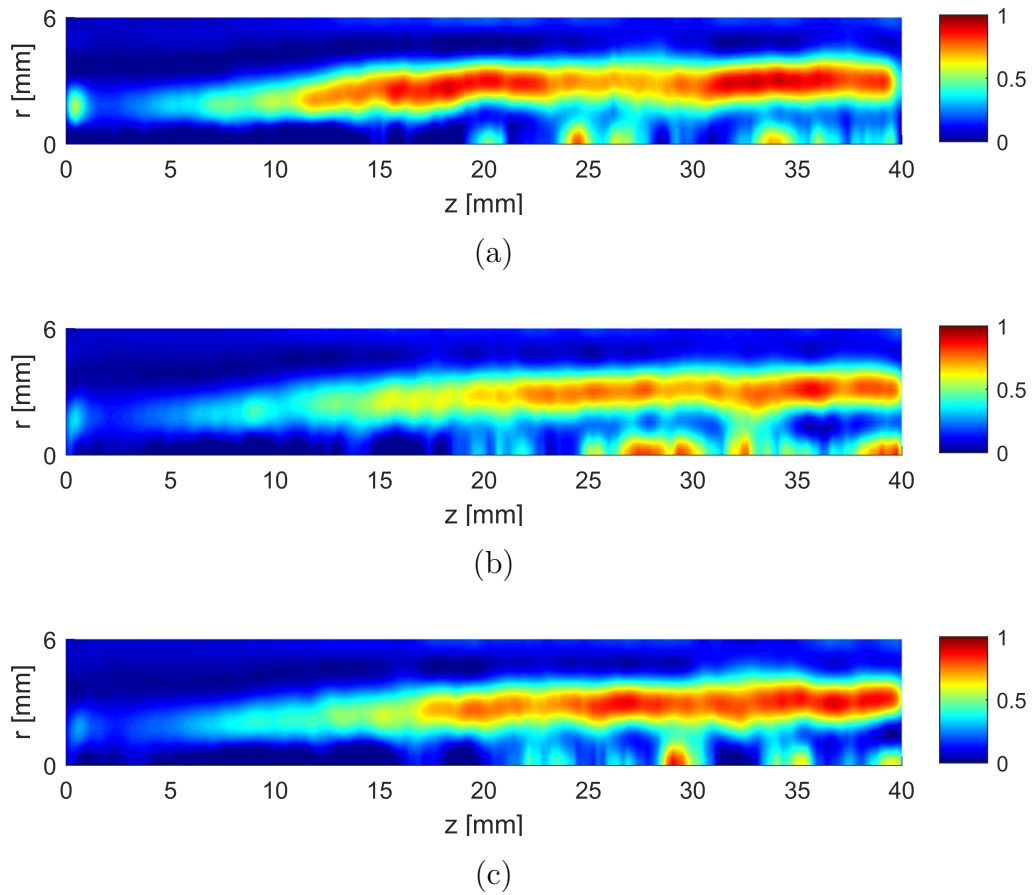


Figure 5.6: Hydrogen: $P_{cc}=20$ bar, ROF (a) 4.4 (b) 5.2 (c) 6.0

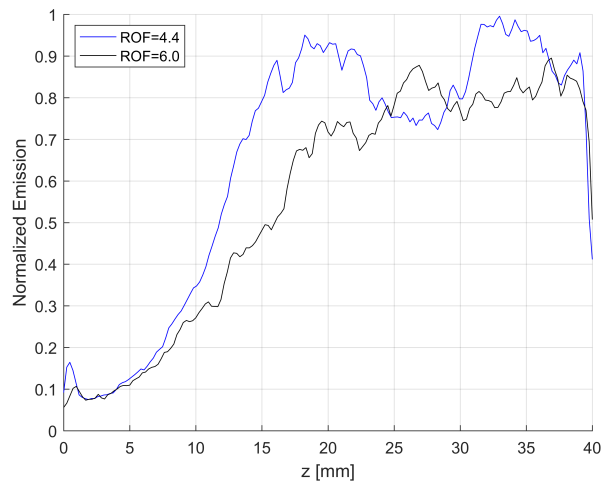


Figure 5.7: Normalized emission development for $P_{cc} = 20$ bar and $ROF = 4.4, 6.0$ along the axial direction for $r = 3$ mm

The explanation can be found considering the different velocities of H_2 in the different cases. In fact, reference may be made to the velocity ratio VR and the momentum flux ratio J for the test cases, taken from G. Laera's Masterthesis [3] and reported in table 5.2. It can be seen that the VR and J , and then the hydrogen velocity, are higher for the case $ROF = 4.4$ than that for the case $ROF = 6.0$, e.g. increases to the ROF decrease.

	VR	J
ROF=4.4	5.158	1.680
ROF=5.2	4.691	1.379
ROF=6.0	4.138	1.078

Table 5.2: Velocity ratio VR and flux ratio for different ROF and Hydrogen case

According to Lux et al. [23], an increase of velocity ratio VR and the momentum flux ratio J at constant chamber pressure involves an increase of OH emission intensity near the injection because of an increase in the shear force between the flows, with a consequent improvement in the mixing.

This is also in agreement with the results of Smith et al. [25] who have seen that for three different relative pressures P_r exists a relationship between the OH emission intensity and the injection velocity ratio VR . Particularly, for the $P_r < 1$, as for the pressure 10 and 20 bar, corresponding to the phase 3 of their tests, such relationship is linear

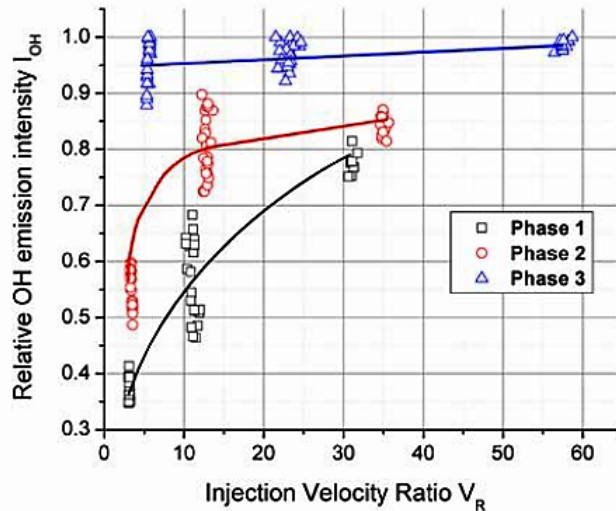


Figure 5.8: Flame relative OH emission intensity as a function of injection velocity ratio and operating phase [25]

However it can be seen that at a certain distance from the injection plane the emission for $ROF = 6.0$ increases more than $ROF = 4.4$ and in some points along the axial direction overcomes it.

Because of the restricted size of the optical window it is not possible determine in what position the overcoming will definitely take place, but it is expected that it will happen because the $ROF = 6.0$ is closer to stoichiometric ratio.

Another effect of the ROF variation, and then of VR and J, can be seen considering the comparison between the radial profiles for example for test case ROF 4.4 and 6.0 at a fixed axial position $z=30$ mm, reported in fig. 5.9

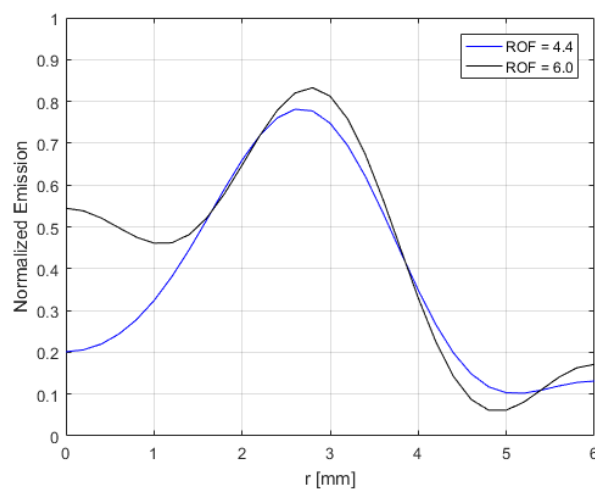


Figure 5.9: Hydrogen: emission radial profiles comparison for $P_{cc}=20$ bar between test case ROF=4.4 and 6.0 at fixed axial position $z=30$ mm

Omitting the wrong values at outer boundary due to the problems already explained in section page 39, a decrease of the flame thickness and the spreading angle can be seen for test case ROF=6.0 respect to ROF=4.4

This trend is again explained considering that an ROF increase involves a decrease of Hydrogen velocity which is pulled inward by faster oxygen, leading to a constriction of the flame and a decrease of the spreading angle.

This result is in agreement with the results of J.J. Smith et al. [26] which have observed that for pressure below the critical point, as is the case, a VR and J decrease, as well as reducing the emission in the near injection area, involves a decrease of the flame thickness.

5.2 Methane

About the GOX/GCH_4 the reconstructed emission radial distributions to the change of P_{cc} and ROF are represented in figs. 5.10 and 5.11

As already said, to highlight the flame shape and anchoring the emission intensities are normalized with the maximum value detected for all ROF test cases and reported in 5.1

- $P_{cc} = 10$ bar

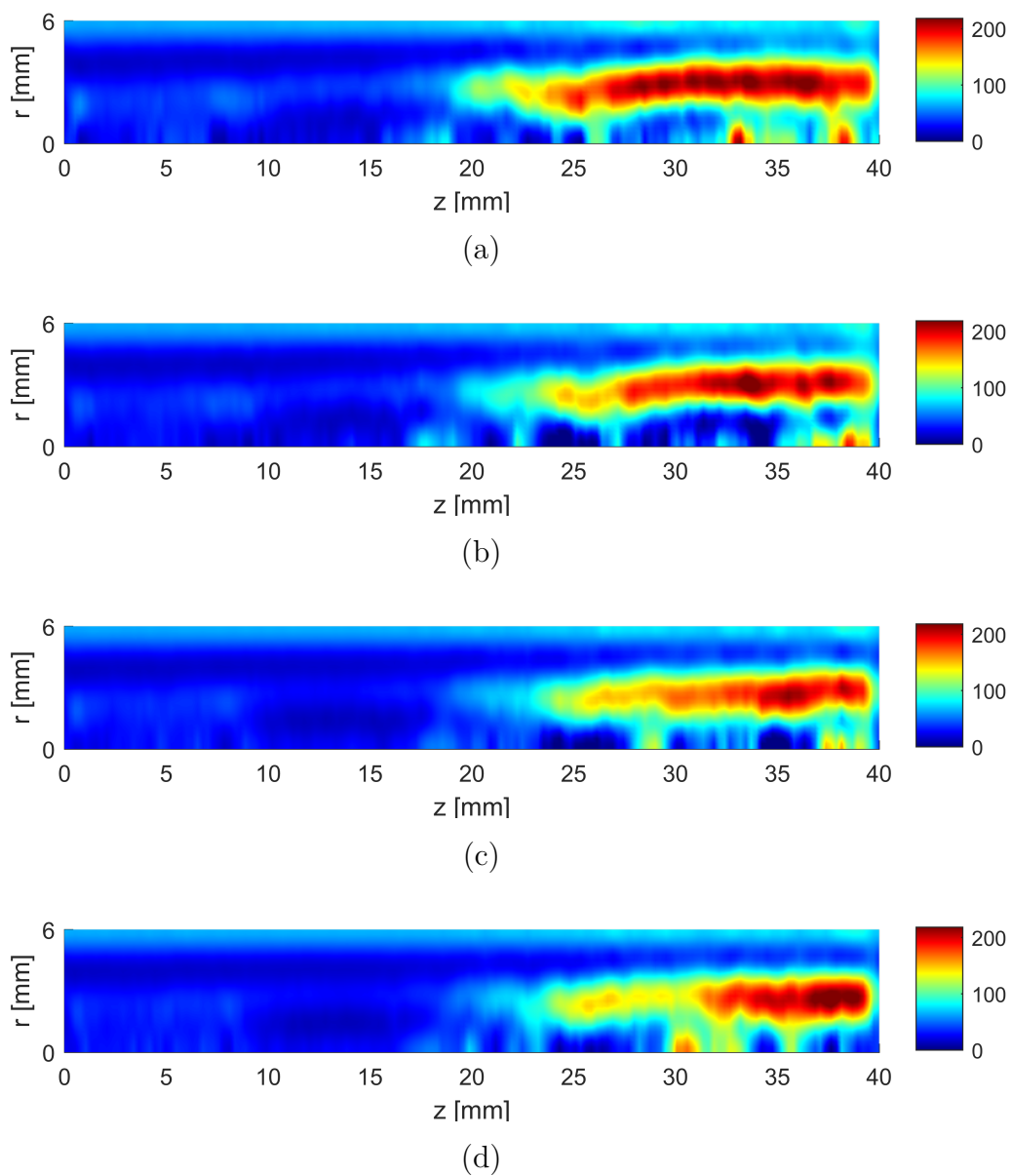


Figure 5.10: Methane $P_{cc}=10$ bar (a) $ROF=2.2$ (b) 2.6 (c) 3.0 (d) 3.4

- $P_{cc} = 20$ bar

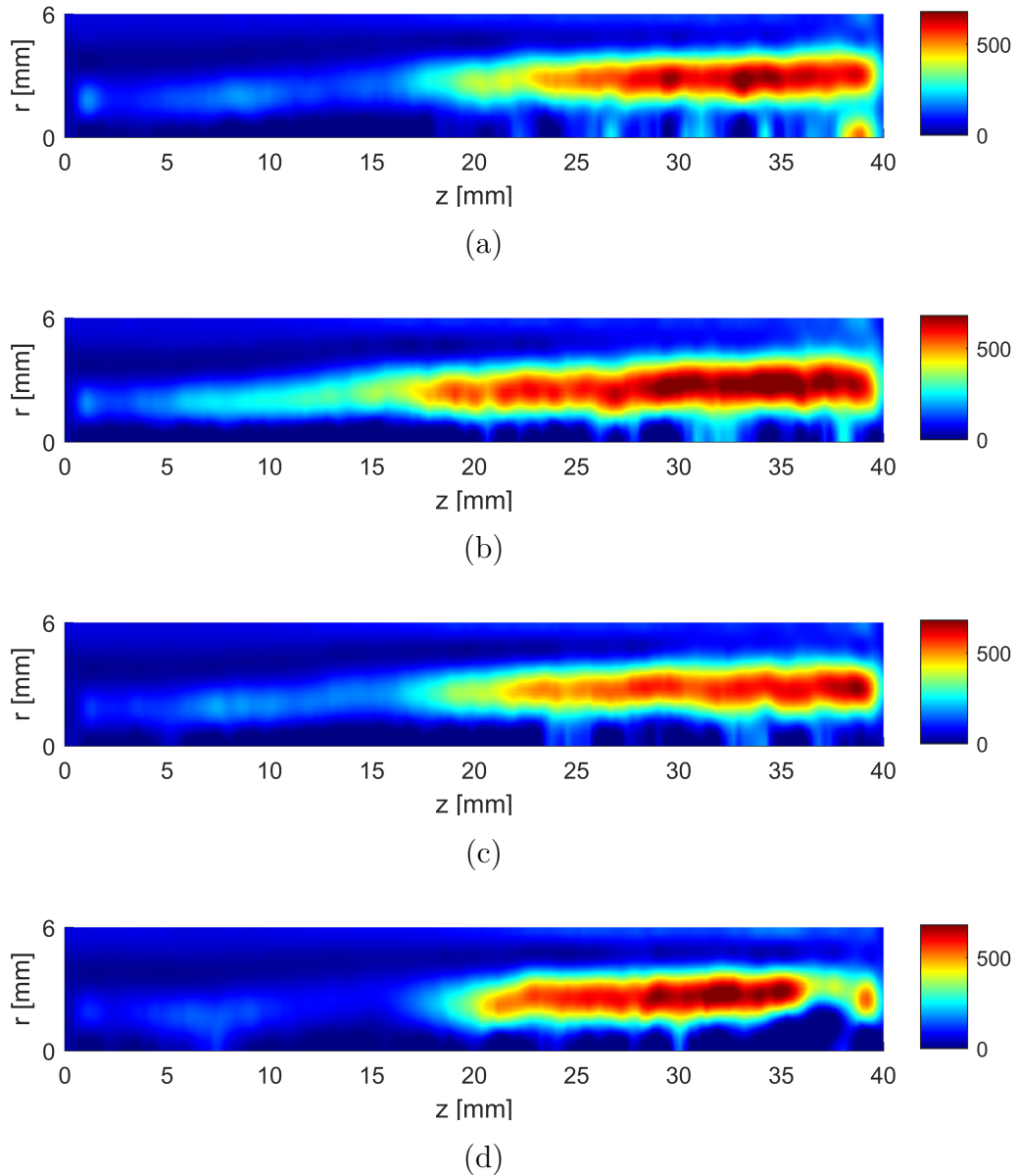


Figure 5.11: Methane $P_{cc}=20$ bar (a) $ROF=2.2$ (b) 2.6 (c) 3.0 (d) 3.4

Note that the decrease of the emission in the end of the window for the test case $P_{cc}=20$ bar and $ROF=3.4$ case is due to a crack during the experiment.

The deconvolution of OH^* emission permits to have an idea of the dimension of the reacting shear layer between the gaseous oxygen and the methane, which is seen to grow continuously with the distance from the GOX injection, according to [22].

Compared with those of propellant combination GOX/GH_2 , these results show similar characteristics: in all cases the flame is attached and incloses the oxygen jet and shows the familiar crescent shape, with little emission at the flame base and higher emission at the end of the image.

This is in agreement with the studies performed by Lux and Haidn [22] and Candel et al. [27], for which both for GOH/GCH_4 and for GOX/GH_2 the flame anchors near the GOX post tip, follows the oxygen jet and the flame shows similar development in a more downstream position.

Similarly to GOX/GH_2 flames, the GOX/GCH_4 flame envelops the gaseous oxygen jet immediately after the injection and at an axial distance of about 4-5 times the GOX inlet internal diameter d_i expands radially and moves towards the combustion chamber walls, in agreement with Winter et al. [1]. This can be again explained by the decrease of shear forces between methane and oxygen jet at a certain distance from the injector, according to Lux et al. [22].

This expansion seems to be insensitive to ROF variation, according with the study of Winter et al. [1] and Lux et al. [28], but the OH^* is a function of it.

To make a comparison between different test cases, the emission radial distribution must be normalized with respect to the maximum value for the Methane test cases which has been seen to occur in the test case 20 bar $ROF=2.6$ and it is equal to 679.0374.

Considering for example the development for the test case $ROF=2.6$ for the pressures 10 bar and 20 bar reported in fig 5.12 it is possible to see the pressure effect on the emission

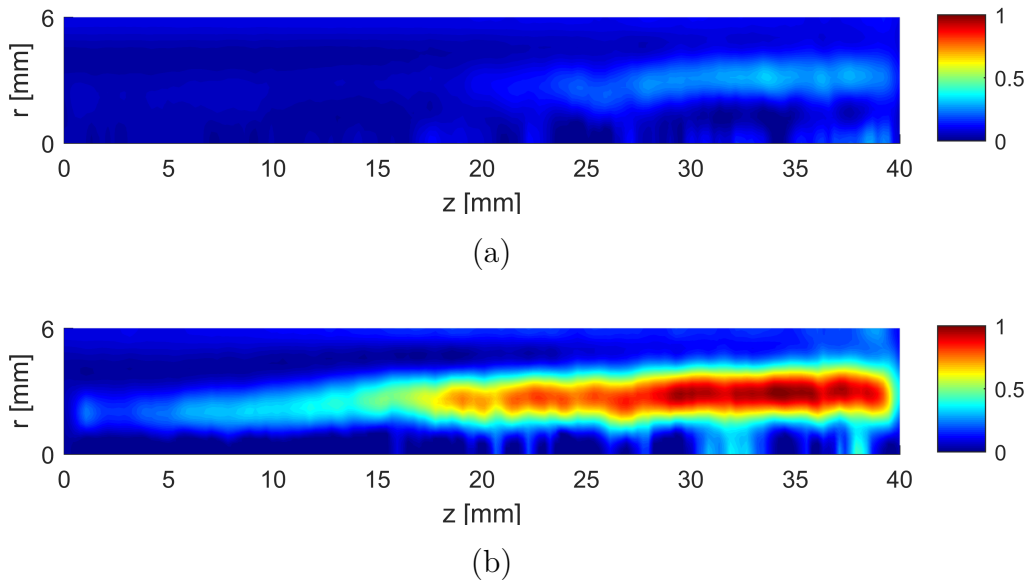


Figure 5.12: Test Methane $ROF=2.6$ (a) 10 bar, (b) 20 bar

Similarly to the GOX/GH_2 , it can be noted that higher pressure translates into a higher emission. To better observe this effect, it can also be considered for the same case the development of the emission along the axial direction for the fixed distance from the flame center $r = 3 \text{ mm}$ represented in fig. 5.13.

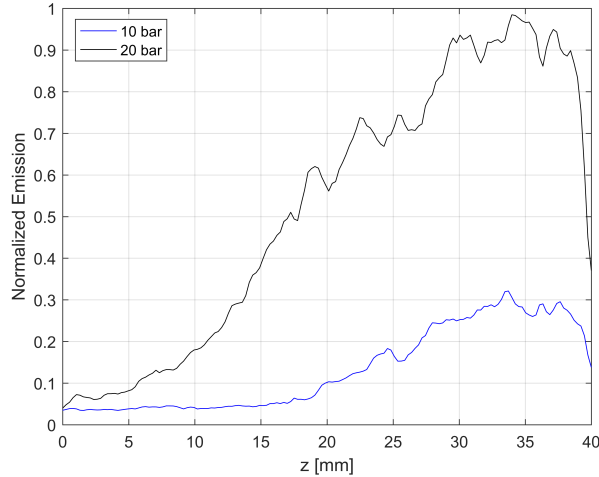


Figure 5.13: Methane : normalized emission development for $ROF = 2.6$ and $P_{cc} = 10 \text{ bar} / 20 \text{ bar}$ along the axial direction for $r = 3 \text{ mm}$

The emission increase with the pressure is according to Johannes Lux and Oskar Haidn [22] whose have studied the flame emission LOX/CH_4 combustion during several steady-state operating points for three pressure levels expressed in terms of the reduced pressure P_r .

They have seen that the emission intensity relates to the combustion chamber pressure and particularly that an increase of pressure is reflected in an increase of emission.

Furthermore, in agreement with the results of Lux et al. [23], an pressure increase at constant VR (and J) results in a constriction of the flame and a slight decrease of the spreading angle. This can be seen in the comparison of emission lateral profile for the fixed axial position $z = 33 \text{ mm}$ for the Methane test case $ROF=2.6$ pressure 10 bar and 20 bar reported in fig. 5.14. Each profile has been normalized with the respective maximum value to enable the comparison.

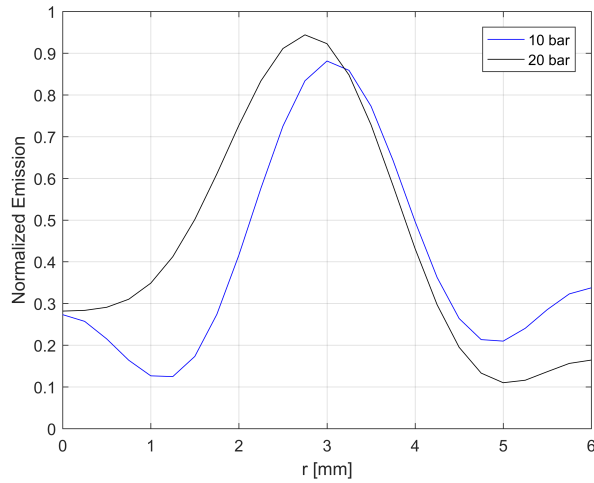


Figure 5.14: Methane: comparison of radial normalized emission for axial position $z = 33mm$ and $ROF = 2.6$ for $P_{cc}=10$ bar/ 20 bar

About the ROF effect on the emission, it is possible to consider the normalized deconvoluted OH^* emission images for a pressure of 20 bar and different ROF , reported in Fig. 5.15.

Note that, similarly to GOX/GH_2 flames, the GOX/GCH_4 flame emission intensities values within a certain distance from the GOX injector are higher for the case with lower ROF , particularly $ROF = 2.6$, with respect to the case $ROF = 3.4$, also if the latter is closer to the ROF stoichiometric value. This can be noted better in fig. 5.16, in which is reported the normalized emission development along the axial direction for a fixed radial position $r = 3 mm$ for the $ROF = 2.6$ and $ROF = 3.4$ cases.

It can be explained considering that the velocity of the methane jet for the 3.4 case is lower than 2.6 case, particularly is the lowest between the four cases as it is possible to see in table 5.3, where are represented the VR and J values taken by Pasquale Difficile's Masterthesis [2]

	VR	J
ROF=2.2	1.268	0.855
ROF=2.6	1.087	0.619
ROF=3.0	0.91	0.433
ROF=3.4	0.83	0.361

Table 5.3: Methane: Velocity ratio VR and momentum flux ratio J for different ROF

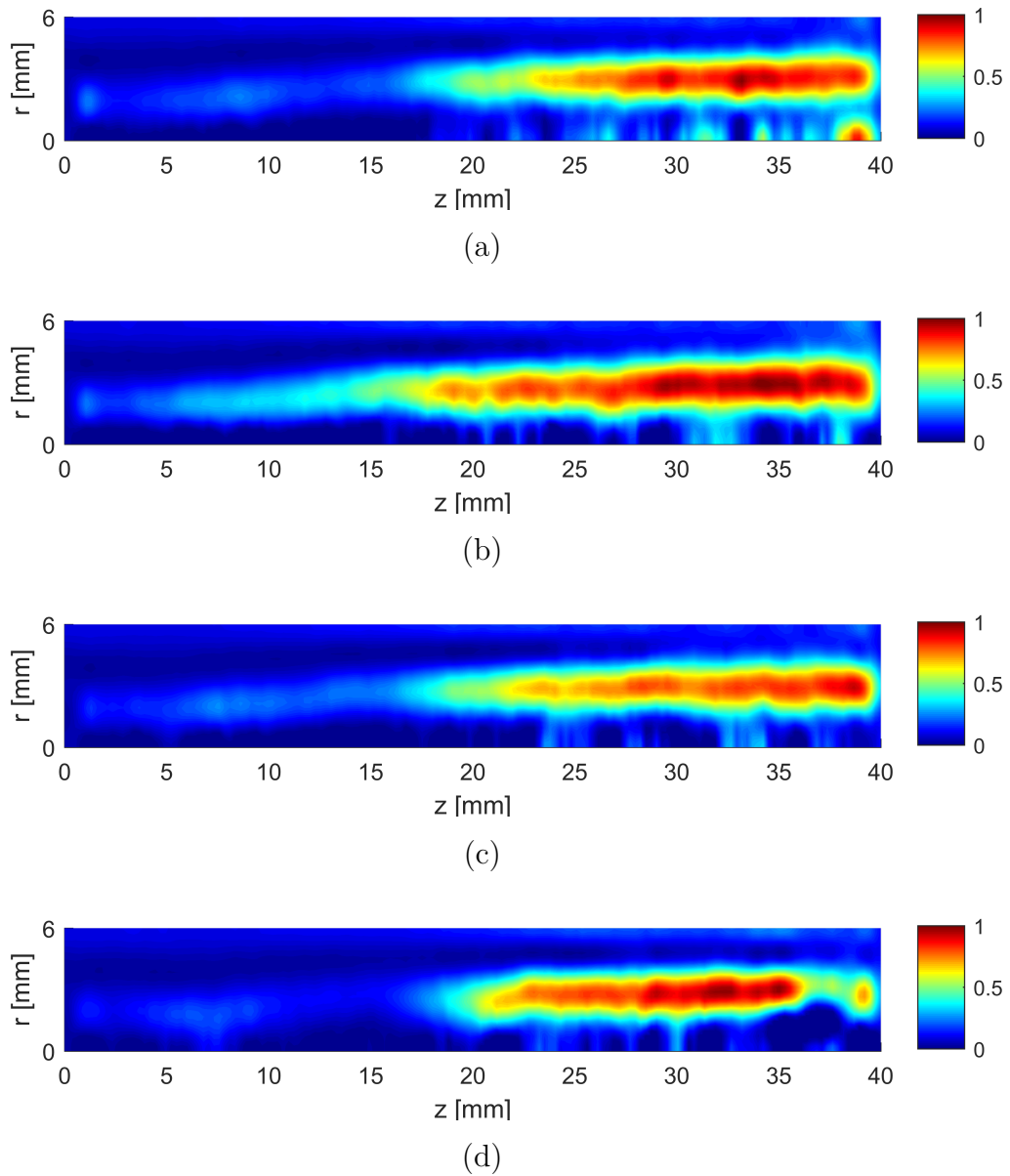


Figure 5.15: Test Methane 20 bar ROF (a) 2.2 (b) 2.6 (c) 3.0 (d) 3.4

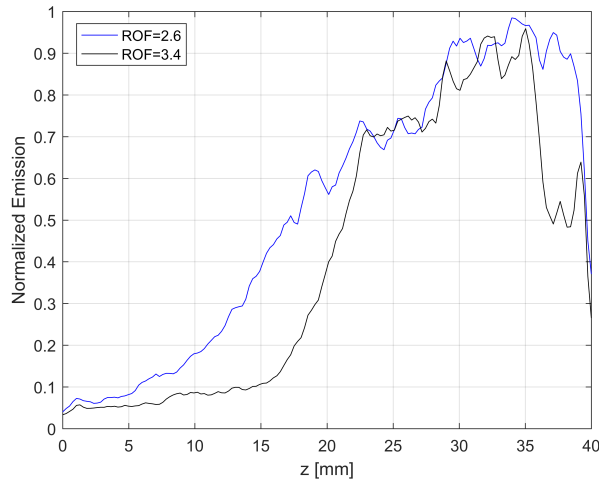


Figure 5.16: Methane: comparison normalized emission along axial direction for fixed lateral position $r = 3 \text{ mm}$, $P_{cc}=20 \text{ bar}$ and $ROF=2.6, 3.4$

According with Lux et al. [23] an higher injection velocity ratio VR and the momentum flux ratio J at constant chamber pressure increases the OH emission because implies a more effective mixing. However, it can be seen that along the combustion chamber the emission for 3.4 case tends to increase more than 2.6 case and exceed it in some positions. This is due to the fact the $ROF=3.4$ case is closer to the stoichiometric ratio, therefore it is expected that at a certain position along the combustion chamber its emission will be finally higher than that of $ROF=2.6$ case, but because of restricted size of the window and the noise presence it is no to possible determine in what position.

To confirm this, it is possible to refer at the work of Perakis et al. [29] in which a study of ROF effect on the heat release trend is evaluated considering the its development at 1 mm distance from the wall and along all the combustion chamber. Such results can be used because it has been seen that the heat release and the emission have the same development when varying the ROF. In such study the heat release, represented in Fig. 5.17, for the first 60 mm after the injector plate are higher for the 2.6 case and the lowest for the 3.4 case. This is due again to the fact that the velocity of the methane for 3.4 case is the lowest, but the reasons are different, because in this case the annular CH_4 jet is pulled inward by the faster O_2 jet due to shear forces, while the flame fluctuations are predominated in the shear layer between the propellants, increasing then the distance of the flame front from the wall. For the case 2.6 the fact that the methane jet has the highest velocity, higher than the oxygen jet, means that the inner oxygen jet is pulled outward, while the flame fluctuations are more pronounced than the 3.4 case. Downstream where the initial mixing effect is dumped, the emission values rise and become the highest for

the 3.4 case because it is closer to the stoichiometric ratio.

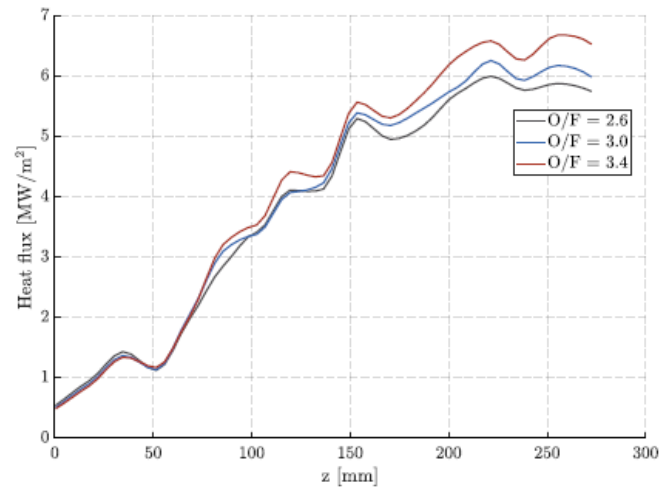


Figure 5.17: Profile of average heat flux at 1 mm distance from the hot gas wall along the axial position

Furthermore, the differences in the velocities and relative flame fluctuations make that the flame is slightly thicker for ROF=2.6 compared to ROF=3.4. It is possible to see what was said considering the shape of the flame varying the radius at a fixed axial position $z = 30 \text{ mm}$ in fig. 5.18

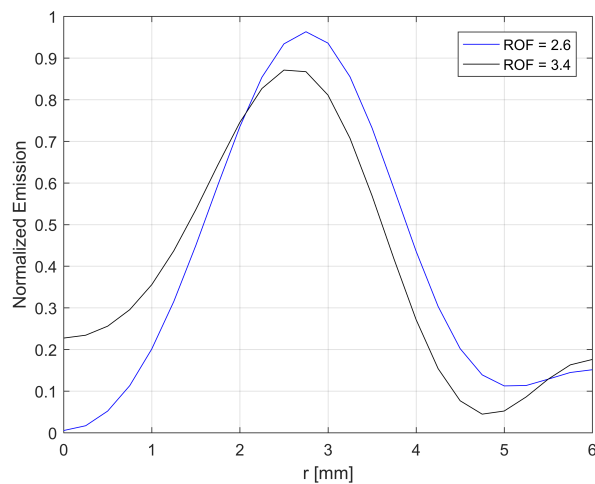


Figure 5.18: Methane: emission radial profiles comparison for $P_{cc}=20$ bar between test cases $ROF=2.6$ and 3.4 at fixed axial position $z=30 \text{ mm}$

5.3 Experimental data vs numerical data

Additionally, the radial profiles obtained with the inverse Abel transform can directly be compared with the flame computational fluid dynamics simulation performed in the same near injection area to validate the results.

Note that the OH^* emission is not a common numerical simulation result, so the comparison between them is limited, but nevertheless the OH^* experimental emission was often compared with simulated OH molar concentration or mass fractions as an approximation [30].

According to Fiala, it can be seen that in flames typical to rocket combustion, if exists a thermal equilibrium between OH^* and OH , it is possible to compute the OH^* molar concentration and therefore OH^* radiation.

This is due to the fact that if the gas is assumed to be optically thin, the OH^* radiation is proportional to the molar concentration of OH^* .

What has been said allows to compare the experimentally obtained OH^* radiation with a numerical OH^* molar concentration, therefore the comparison for the test case Methane pressure 20 bar and ROF=2.6 in Fig. 5.19 can be considered.

More detail about the numerical simulation and how it was obtained are provided by Philipp Burggraf's Semester thesis [31], which has performed it.

To allow the comparison between the images, a different colormap was used respect to the image previously presented and each of them has been normalized respect to the relative maximum value that occurs in the numerical simulation and radial distribution reconstruction.

Because in the experiment only some pixels record a certain maximum emission value, if such value is used for the normalization, the resulting flame appears to be not uniform compared to that of numerical simulation. Then, it was thought to introduce a cutoff emission value equal to 0.8 of maximum emission value found in the recovered radial distribution in order to have a more uniform flame comparable with the simulation flame. Furthermore, because of the window reflection non zero emission values are present at the boundary in the experimental reconstruction with respect to the numerical simulation because such problems obviously are not present .

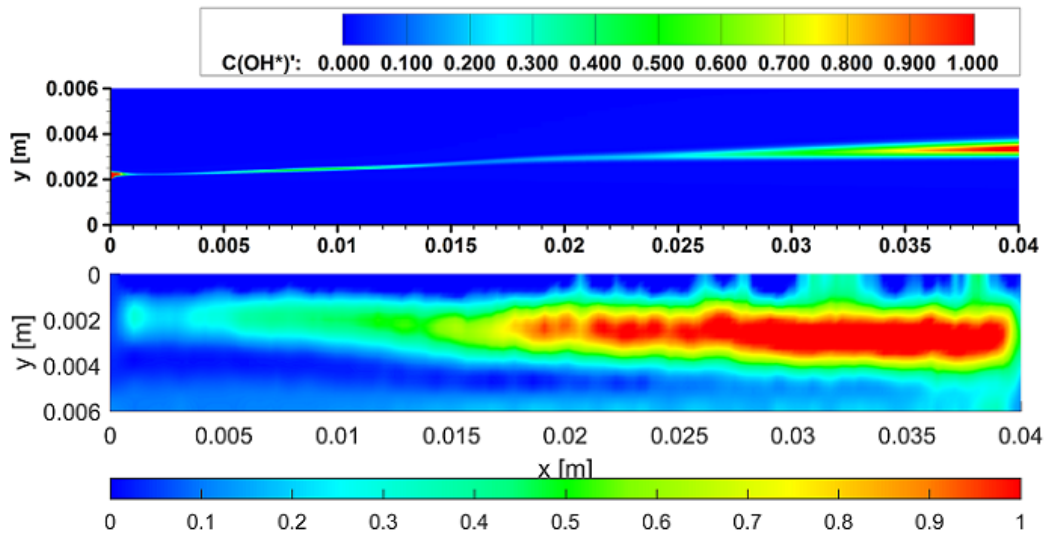


Figure 5.19: Comparison numerical vs experimental

From the image can be seen that the assumption of an optically thin gas appears justified, then the OH^* radiation is proportional to the molar concentration of OH^* .

This can be seen from the images where at an increase in the normalized OH^* molar concentration is associated an increase of the normalized OH^* emission.

Furthermore, note that both the flames have a similar typical trend already discussed: they are attached, inclose the oxygen jet and at an axial distance of about 5-6 times the GOX injector diameter the flame expands radially showing a crescent shape with a little emission at the flame base and higher at the end.

For what has been said, the experimental radiation data seem to be in agreement with the numerical data. The unique substantial differences concern the fact that the maximum value of OH^* molar concentration for the numerical simulation is shown to be achieved much further downstream and the flame is thinner with respect to the OH^* experimental emission.

However, these differences can be due substantially to the fact that the numerical model unpredict the flame thickness and therefore improvements in the OH^* emission prediction are necessary.

Chapter 6

Conclusions & Outlook

In the context of the optical diagnostics, the Chemiluminescence method has been used to study the combustion process by means of the detection of the spontaneous OH^* radiation. To have local informations about it, an Inverse Abel transform code has been implemented to recover the emission radial distribution. The code has been checked with known radial distribution and lateral distribution functions and has been applied to the experimental intensity images recorded by an ICCD camera. The results seem to be in agreement with the typical combustion process behavior of the propellant pair GOX/GCH_4 and GOX/GH_2 , already widely studied in the literature, and this confirms the correctness of the code. Furthermore, such results match well with also the numerical simulations data, and therefore the code is further validated.

Nevertheless, it was observed that in the reconstruction some negative emission values are present probably due to asymmetries and not correct flame center detection. So an appropriate symmetrization and flame center detection techniques are required to be added to the code in the future works.

To reinforce further the code and improve the results, greater attention can be given to the identification of the frequencies to which the experimental noise is localized. Furthermore, an improvement of the post-processing phase is required to get better results from the inverse Abel transform.

Chapter 7

Acknowledgments

I would like initially to thank my supervisor Fernanda Winter for giving me the chance to do this experience in a context, that of scientific research, and in a nation unknown to me. Thank you for your availability and for the patience offered to me in each moment of these months. I have grown and improved a lot and owe it to her too. I want to thank the professor Dario G. Pastrone who has personally committed himself and has allowed me to live this life experience. My thanks are also addressed to Professor Oskar J. Haidn and to all those working at the Lehrstuhl für Flugantriebe of the Technische Universität München for giving me the opportunity to learn from them.

I would like to thank my friends, Alessandro Villani and Pasquale Difficile, with whom I lived and with whom I overcame the difficulties encountered. Without them, probably it would not have been in the same way.

Finally, i would like to thank my family, my dad Cosimo, my mom Rosaria and my brothers Giovanni e Simone. Without their support and their sacrifices none of this would have happened. Thank you.

Bibliography

- [1] F. F. Winter, S. Silvestri, M. Celano, G. Schlieben, and O. Haidn, “High-speed and emission imaging of a coaxial single element gox/gch4 rocket combustion chamber,” in *European Conference for Aeronautics and Space Sciences*, 2017.
- [2] P. Difficile, “Performance and emission imaging of a coaxial single element g02/gch4 rocket combustion chamber,” *Master thesis*, 2018.
- [3] G. Laera, “Emission imaging of a coaxial single element g02/gch4 rocket combustion chamber,” *Master thesis*, 2018.
- [4] I. TSI, “Advanced combustion diagnostics (2013),”
- [5] T. Fiala, *Radiation from high pressure hydrogen-oxygen flames and its use in assessing rocket combustion instability*. Verlag Dr. Hut, 2015.
- [6] M. Zhao, R. Choudhury, R. Malpress, and D. Buttsworth, “Absolute concentration measurements of oh^* in an axisymmetric hydrogen-air premixed flame adjacent to a hot graphite model,” in *Proceedings of the 20th Australasian Fluid Mechanics Conference*, Australasian Fluid Mechanics Society, 2016.
- [7] J. Runyon, R. Marsh, Y. A. Sevcenco, D. Pugh, and S. Morris, “Development and commissioning of a chemiluminescence imaging system for an optically-accessible high-pressure generic swirl burner,” 2015.
- [8] H. Fulge, A. Knapp, R. Wernitz, C. Eichhorn, G. Herdrich, S. Fasoulas, and S. Lohle, “Improved abel inversion method for analysis of spectral and photo-optical data of magnetic influenced plasma flows,” in *42nd AIAA Plasmadynamics and Lasers Conference in conjunction with the 18th International Conference on MHD Energy Conversion (ICMHD)*, p. 3456, 2011.
- [9] R. K. Pandey, S. Suman, K. K. Singh, and O. P. Singh, “An approximate method for abel inversion using chebyshev polynomials,” *Applied Mathematics and Computation*, vol. 237, pp. 120–132, 2014.

-
- [10] S. Ma, H. Gao, G. Zhang, and L. Wu, “A versatile analytical expression for the inverse abel transform applied to experimental data with noise,” *Applied spectroscopy*, vol. 62, no. 6, pp. 701–707, 2008.
- [11] R. Alvarez, A. Rodero, and M. Quintero, “An abel inversion method for radially resolved measurements in the axial injection torch,” *Spectrochimica Acta Part B: Atomic Spectroscopy*, vol. 57, no. 11, pp. 1665–1680, 2002.
- [12] H. K. Park, “Error analysis of a new asymmetric abel-inversion method,” *Review of Scientific Instruments*, vol. 61, no. 10, pp. 2879–2881, 1990.
- [13] G. Pretzier, H. Jäger, T. Neger, H. Philipp, and J. Woisetschläger, “Comparison of different methods of abel inversion using computer simulated and experimental side-on data,” *Zeitschrift für Naturforschung A*, vol. 47, no. 9, pp. 955–970, 1992.
- [14] G. Pretzier, “A new method for numerical abel-inversion,” *Zeitschrift für Naturforschung A*, vol. 46, no. 7, pp. 639–641, 1991.
- [15] S. Ma, H. Gao, and L. Wu, “Modified fourier-hankel method based on analysis of errors in abel inversion using fourier transform techniques,” *Applied optics*, vol. 47, no. 9, pp. 1350–1357, 2008.
- [16] V. Dribinski, A. Ossadtchi, V. A. Mandelshtam, and H. Reisler, “Reconstruction of abel-transformable images: The gaussian basis-set expansion abel transform method,” *Review of Scientific Instruments*, vol. 73, no. 7, pp. 2634–2642, 2002.
- [17] C.Killer, “Abel inversion algorithm, matlab, central file exchange, <https://de.mathworks.com/matlabcentral/fileexchange/43639-abel-inversion-algorithm>,”
- [18] M. Buie, J. Pender, J. Holloway, T. Vincent, P. Ventzek, and M. Brake, “Abel’s inversion applied to experimental spectroscopic data with off axis peaks,” *Journal of Quantitative Spectroscopy and Radiative Transfer*, vol. 55, no. 2, pp. 231–243, 1996.
- [19] G. C.-Y. Chan and G. M. Hieftje, “Estimation of confidence intervals for radial emissivity and optimization of data treatment techniques in abel inversion,” *Spectrochimica Acta Part B: Atomic Spectroscopy*, vol. 61, no. 1, pp. 31–41, 2006.
- [20] M. Apostolopoulos, M. Taroudakis, and D. Papazoglou, “Application of inverse abel techniques in in-line holographic microscopy,” *Optics Communications*, vol. 296, pp. 25–34, 2013.

-
- [21] J. Altenberend, “Kinetics of the plasma refining process of silicon for solar cells: experimental study with spectroscopy,” *Grenoble university*, 2012.
- [22] J. Lux and O. Haidn, “Flame stabilization in high-pressure liquid oxygen/methane rocket engine combustion,” *Journal of Propulsion and Power*, vol. 25, no. 1, pp. 15–23, 2009.
- [23] J. Lux, D. Suslov, M. Bechle, M. Oswald, and O. Haidn, “Investigation of sub-and supercritical lox/methane injection using optical diagnostics,” in *42nd AIAA/ASME/SAE/ASEE Joint Propulsion Conference & Exhibit*, p. 5077, 2006.
- [24] R. Stützer, T. Fiala, and M. Oswald, “The pressure dependence of optical flame emission from space propulsion-relevant hydrogen combustion,” in *7th European Conference for Aeronautics and Space Sciences*, 2017.
- [25] J. J. Smith, G. Schneider, D. Suslov, M. Oswald, and O. Haidn, “Steady-state high pressure lox/h₂ rocket engine combustion,” *Aerospace Science and Technology*, vol. 11, no. 1, pp. 39–47, 2007.
- [26] J. Smith, D. Suslov, M. Oswald, O. Haidn, and M. Bechle, “High pressure lox/h₂ combustion and flame dynamics,” in *40th AIAA/ASME/SAE/ASEE Joint Propulsion Conference and Exhibit*, p. 3376, 2004.
- [27] S. CANDEL*, M. Juniper, G. Singla, P. Scoufflaire, and C. Rolon, “Structure and dynamics of cryogenic flames at supercritical pressure,” *Combustion Science and Technology*, vol. 178, no. 1-3, pp. 161–192, 2006.
- [28] J. Lux and O. Haidn, “Effect of recess in high-pressure liquid oxygen/methane coaxial injection and combustion,” *Journal of Propulsion and Power*, vol. 25, no. 1, pp. 24–32, 2009.
- [29] N. Perakis, M. P. Celano, and O. J. Haidn, “Heat flux and temperature evaluation in a rectangular multi-element gox/gch₄ combustion chamber using an inverse heat conduction method,” in *7th European Conference for Aerospace Sciences*, 2017.
- [30] T. Fiala and T. Sattelmayer, “A posteriori computation of oh* radiation from numerical simulations in rocket combustion chambers,” in *5th European Conference for Aeronautics and Space Sciences (EUCASS), Munich, July*, pp. 1–5, 2013.
- [31] P. BURGGRAF, “Numerical investigation of combustion and heat transfer in a g₀₂/gch₄ single element rocket combustion chamber,” *Semester thesis*, 2018.

Appendix A

Appendix

A.1 Inverse Abel Transform code

```
1 %% INVERSE ABEL TRANSFORM CODE
2
3 %% The code is based on Fourier Method, described in
4 %% "A New Method for Numeric Abel-Inversion", Georg Pretzler,
5 %% Z. Naturforsch. 46a, 639 - 641 (1991);
6
7 clc ; clear all ; close all ;
8
9 %% Loading image and data extraction
10
11 % METHANE
12
13 % open('AverageWindowed_Met_10bar_2.2.fig');           % Open Image
14 % open('AverageWindowed_Met_10bar_2.6.fig');           % Open Image
15 % open('AverageWindowed_Met_10bar_3.0.fig');           % Open Image
16 % open('AverageWindowed_Met_10bar_3.4.fig');           % Open Image
17 % open('AverageWindowed_Met_20bar_2.2.fig');           % Open Image
18 open('AverageWindowed_Met_20bar_2.6.fig');           % Open Image
19 % open('AverageWindowed_Met_20bar_3.0.fig');           % Open Image
20 % open('AverageWindowed_Met_20bar_3.4.fig');           % Open Image
21
22 % HYDROGEN
23
```

```
24 % open('AverageWindowed_Hyd_10bar_4.4.fig');           % Open Image
25 % open('AverageWindowed_Hyd_10bar_5.2.fig');           % Open Image
26 % open('AverageWindowed_Hyd_10bar_6.0.fig');           % Open Image
27 % open('AverageWindowed_Hyd_10bar_6.8.fig');           % Open Image
28 % open('AverageWindowed_Hyd_20bar_4.4.fig');           % Open Image
29 % open('AverageWindowed_Hyd_20bar_5.2.fig');           % Open Image
30 % open('AverageWindowed_Hyd_20bar_6.0.fig');           % Open Image
31
32 % Allocation of loaded image in the figure h
33 h=gcf;
34
35 % Extraction data from the figure h:
36 % Image axes and values are allocated in the dataObj cell
37 axesObj=get(h,'Children');
38 dataObj=get(axesObj,'Children');
39
40 % Extraction of the pixels/values number of the image along
41 % axial direction from the data vector
42 xdata=get(dataObj{2},'XData');
43
44 % Extraction of the pixels/values number of the image along
45 % lateral direction from the data vector
46 ydata=get(dataObj{2},'YData');
47
48 % Extraction of the intensities matrix from the data vector
49 zdata=get(dataObj{2},'CData');
50
51 % Mesh construction along the axial direction of the image:
52 % the z-vector goes from 0 mm to 40 mm and the points number
53 % will be equal to the pixels number in that direction
54 z=linspace(0,40,xdata(end));
55
56 % Mesh construction along the lateral direction of the image:
57 % the y-vector goes from 0 mm to 12 mm and the points number
58 % will be equal to the pixels number in that direction
59 y=linspace(0,12,ydata(end));
```

```
60
61 % The normalized images are provided from the experimental
    part
62 % Each image have to be multiplied by the value of
    normalization
63 zdata=zdata*5289.4; % 5289.4 Methane % 5723 Hydrogen
64 zdata=fliplr(zdata);
65
66 % Creation of the 2D mesh
67 [Z,Y]=meshgrid(z,y);
68
69 % Plot of the intensity image
70 figure(1)
71 surf(Z,Y,zdata)
72 colormap(jet)
73 xlabel('z [mm]')
74 ylabel('y [mm]')
75 shading interp
76 axis equal
77 axis([0 40 0 12])
78 title('Intensity')
79
80 %% Construction of average image
81
82 % Since different images can have odd or even pixels number
83 % in lateral direction, it is necessary differentiate the
84 % two cases to obtain the average image by means of an if-
85 % else command
86
87 % if the vector y has an odd number of values
88 if mod(length(y),2) ~ 0
89
90 % The intensity values on the flame center for each station
91 % along the axial direction
92 fcentro= zdata(ceil(length(y)/2),:);
93
```

```
94 % The intensity values of image upper half
95 fupper=zdata(ceil(length(y)/2)+1:end,:);
96
97 % The intensity values of image down half
98 fdown=zdata(1:ceil(length(y)/2)-1,:);
99
100 % Rotation of the down of the image to add the upper half and
101 % the down half values equidistant from the flame center and
102 % obtain the average image
103
104 for j=1:length(zdata(1,:))
105
106     fdown(:,j)=fliplr(fdown(:,j)');
107
108 end
109
110 % if instead the vector y has an even number of values, the
111 % intensity values on the flame center is not present, but
112 % it is possible to obtain it with an linear interpolation
113 % between the neighboring values. This interpolation is
114 % extended to every position along axial direction
115
116 else
117
118     for j=1:length(z)
119
120 % Linear interpolation to calculate the intensity values on
121 % the flame center
122         s=polyfit([y(end/2) y(end/2+1)],[ zdata(end/2,j)
123             zdata(end/2+1,j)],1);
124         fcentro(j)=polyval(s,(y(end/2)+ y(end/2+1))/2);
125     end
126
127 % The intensity values of image upper half
128 fupper=zdata(ceil(length(y)/2)+1:end,:);
```

```
129
130 % The intensity values of image down half
131 fdown =zdata(1:ceil(length(y)/2),:);
132
133 % Rotation of the down half of the image to average the upper
134 % half and the down half values equidistant from the flame
135 % center and obtain the average image
136
137     for j=1:length(zdata(1,:))
138
139         fdown(:,j)=fliplr(fdown(:,j)');
140
141     end
142
143 end
144
145 % Construction of the average image by means the average
146 % profiles at each station along axial direction. The
147 % calculation is valid both even and odd pixels number
148
149 for j=1:length(z)
150
151     fMedia(:,j)=[fcentro(j); (fdown(:,j)+fupper(:,j))/2];
152
153 end
154
155 % Definition of the radius vector r by means of mesh
156 % construction along the lateral direction: the radius
157 % goes from the flame center 0 mm to the upper combustion
158 % chamber wall, distant 6 mm from the flame center, and
159 % the values number of it is equal to values number of
160 % average image along the lateral direction
161 r=linspace(0,6,length(fMedia(:,1)));
162
163
164 figure(2)
```

```
165 surf(z,r,fMedia)
166 colormap(jet)
167 xlabel('z [mm]')
168 ylabel('r [mm]')
169 shading interp
170 axis equal
171 axis([0 40 0 6])
172 title('Average image')
173
174
175 % The maximum radius will be posed higher than the last
176 % value of r to avoid the singularity in the Abel transform
177 % integral when y=r
178 R=6+0.001;
179
180 %% Application of G.Pretzler procedure
181
182 % Definition of expansion frequencies
183 lof=1;    % Lower frequency of expansion
184 upf=4;    % Upper frequency of expansion
185
186 % Definition of the fnM cosine-functions set. The rows are
187 % the y-values columns are the number of expansion elements,
188 % equal n+1 since we start with n=0
189 fnM=zeros(length(r),upf+1);
190
191 % Definition of the hnM quantities obtained by means of the
192 % direct Abel transform applicated to fnM
193 hnM=zeros(length(r),upf+1);
194
195 %% Calculation of the fnM and hnM matrices
196
197 % Particular case : for expansion number n=0, fn_0 =1
198 fnM(:,1)=1;
199
200 for c=1:length(r);
```

```

201
202     yy=r(c);
203
204 % Definition of the function that must be integrated in the
205 % direct Abel transform for n=0
206     funM = @(t) 2.*t./sqrt(t.^2-yy.^2);
207
208 % Application of the direct Abel transform to the funM
209     hnM(c,1) = integral(funM,yy,R);
210
211 end
212
213
214 % For all other columns, e.g. for all other expansion numbers
215 for n=1:upf
216
217     for c=1:length(r)
218
219         yy=r(c);
220
221 % Calculation of the cosine function fnM
222         fnM(c,n+1) = (1 - (-1)^n*cos(n*pi*yy/R));
223
224 % Definition of the function that must be integrated in the
225 % direct Abel transform for n different from zero
226         funM= @(t) 2.*(1 - (-1)^n*cos(n*pi.*t/R)).*t./sqrt(t
                .^2-yy.^2);
227
228 % Application of the direct Abel transform to the funM
229         hnM(c,n+1) = integral(funM,yy,R);
230
231     end
232
233 end
234
235 %% Calculation of the unknown amplitudes matrix AM

```

```

236
237 % In the 1D case the H vector is the Abel transform
238 % applicated to  $f(r) = \sum_{n=lof}^{upf} (A_n * f_n(r))$  ,
239 % while the h(y) is the real data vector.
240 % Using the least squares method to fit H(y) to the real
241 % data h(y) :
242 %  $\sum_{k=1}^N (H(y_k) - h(y_k))^2 = \min$ 
243 % where N is the number of points used along the lateral
244 % direction y , it leads to:
245
246 %  $\sum_{n=lof}^{upf} A_n * \sum_{k=1}^N (hnM_n(y_k) * hnM_m(y_k))$ 
247 % =  $\sum_{k=1}^N (h(y_k) * hnM_m(y_k))$ 
248 % for each m:  $lof \leq m \leq upf$ 
249
250 %  $AM * CM = BM \rightarrow AM = BM * inv(CM)$ 
251 % that solved allows to obtain the AM amplitudines.
252 % The AM and BM quantities are vectors in the 1D case ,
253 % while they are matrices in the 2D case because station
254 % by station along the axial direction different radial
255 % distributions are present. Similarly the vector of real
256 % data h(y) is replaced by the data matrix extracted from
257 % the projection/image fMedia
258
259 % Definition of the emission radial distribution matrix
260 f_recM=zeros(length(r),length(z));
261 % Definition of the amplitudines matrix AM
262 AM=zeros(length(z),upf+1);
263 % Definition of the matrix BM
264 BM = zeros(length(z),upf+1);
265 % Definition of the matrix CM
266 CM= zeros(upf+1,upf+1);
267
268 % Triple for cycle extended to the stations number
269 % along the axial direction and frequencies number
270 % to calculate CM, BM and AM matrix
271

```

```

272 for j=1:length(z)
273
274     for k=1:upf+1
275
276         for l=1:upf+1
277
278             CM(l,k)=sum(hnM(:,k).*hnM(:,l));
279
280         end
281
282         BM(j,k)= sum(fMedia(:,j).*hnM(:,k));
283
284     end
285 % Inversion of the equation AM * LM = BM
286     AM(j,:)=BM(j,:)*inv(CM);
287
288 end
289
290 %% Radial distribution calculation
291
292 % In the 1D case  $f(r) = \sum_{n=1}^{upf} (A_n * f_n(r))$ ,
293 % In the 2D case the radial distribution will be
294 %  $f(r,z) = \sum_{n=1}^{upf} (A_n(z) * f_n(r,z))$ 
295 % so it is possible to apply the sum valid in the 1D case
296 % to each position along axial direction z by means
297 % a for cycle
298
299 for j=1:length(z)
300 % for the particular case n=0 , fn_0=1
301     f_recM(:,j)= f_recM(:,j) + AM(j,1)*1;
302 % for the other n
303     for c=2:upf+1
304
305         f_recM(:,j) = f_recM(:,j)+ AM(j,c).*fnM(:,c);
306
307     end

```

```
308
309 end
310
311 %% Direct Abel transform
312 % Application of direct Abel transform to the radial
      distribution to
313 % calculate the projection and compare with initial image
314
315 % Allocation of radius vector and radial distribution
316
317 fine=length(r);
318 for j=1:length(z)
319     for i=1:fine
320
321         hhh(i,j)=r(1,i);
322         fff(i,j)=f_recM(i,j);
323
324     end
325 end
326
327 % Interpolation of radial distribution. The interpolating
      polynomial is calculated
328 % at each station along the flame axis obtaining a matrix
329
330 ord=2; % Initial choice of interpolation order
331
332 for j=1:length(z)
333
334     h=polyfit(hhh(:,j),fff(:,j),ord);
335     fpol(:,j)=polyval(h,r); % Interpolating polynomial
      valued at each radius
336
337 end
338
339 % Increase of interpolation order by means of while cycle
      assuring that the
```

```

340 % relative error between the interpolating polynomial and the
      radial
341 % distribution is below a certain value
342
343 for j=1:length(z)
344     ord=2;
345     while abs(max(fpol(:,j)-f_recM(:,j))./max(f_recM(:,j)))>
      0.1
346
347         ord=ord+1;
348         h=polyfit(hhh(:,j),fff(:,j),ord);
349         fpol(:,j)=polyval(h,r);
350     end
351
352 % Creation of continue function by means of interpolating
      polynomial
353 % in order to apply the direct Abel transform.
354
355     tt=@(t,i) t.^i;
356     somma=@(t) h(end).*t.^0;
357     ss=ord;
358
359     for i=1:ord
360
361         funzione=@(t) h(i)*tt(t,ss);
362         somma=@(t) somma(t) + funzione(t);
363         ss=ss-1;
364
365     end
366
367
368     for i=1:length(r)
369
370         xx=r(i);
371         f=@(t) 2.*somma(t).*t./sqrt(t.^2 - xx^2); % function
      in the Abel integral

```

```
372         pro(i,j)= integral(f,xx,R); % direct Abel transform
           in order to have the projection
373
374     end
375 end
376
377
378 % Because of the negative values presence in the emission
379 % radial distribution whose are not physical, such values
380 % are setted to a value close to zero
381
382 f_recMff=(f_recM);
383 f_recMff(f_recMff<0) = 1e-20;
384
385
386 %% Plot
387
388 % Radial distribution
389 figure(3)
390 surf(z,r,f_recMff)
391 colormap(jet)
392 xlabel('z [mm]')
393 ylabel('r [mm]')
394 shading interp
395 axis equal
396 axis([0 40 0 6])
397 title('Radial distribution')
398
399 % For the comparison between different test cases, an
400 % normalized emission radial distribution is obtained
401 % dividing by the maximum value between the same test cases.
402 % For the Methane propellant the maximum value 679.0374 is
403 % obtained in test case 20 bar ROF=2.6 , for the Hydrogen
404 % propellant the maximum value 787.9613 is obtained in test
405 % case 20 bar ROF=4.4
406
```

```
407
408 % Normalized radial distribution
409 figure(4)
410 fnorm=f_recMff/679.0374; % Methane 679.0374 , Hydrogen
    787.9613
411 surf(z,r,fnorm)
412 colormap(jet)
413 xlabel('z [mm]')
414 ylabel('r [mm]')
415 shading interp
416 axis equal
417 axis([0 40 0 6])
418 caxis([0 1])
419 title('Normalized radial distribution')
420
421
422 % Normalized radial distribution for comparison with
    numerical simulation
423 figure(5)
424 load('Rainbow_colormap.mat')
425 f_recMfff=(f_recM);
426 f_recMfff(f_recMfff<0) = 1e-20;
427
428 f_recMfff(f_recMfff>0.8*max(max(f_recMfff))) = 0.8*max(max(
    f_recMfff)); % Application of a cut off value
429 f_recMfff=f_recMfff/(679.0374.*0.8);% Methane 679.0374 ,
    Hydrogen 787.9613
430
431 zz=z/1000;
432 rr=r/1000;
433 surf(zz,rr,f_recMfff)
434 colormap(rainbow_map)
435 xlabel('z [m]')
436 ylabel('y [m]')
437 shading interp
438 axis equal
```

```
439 axis([0 0.04 0 0.006])
440 title('Normalized radial distribution for comparison with
        numerical simulation')
441 caxis([0 1])
442
443 % Comparison between original projection and reconstrued
        projection
444 figure(6)
445 surf(z,r,pro)
446 xlabel('z')
447 ylabel('x')
448 hold on
449 surf(z,r,fMedia)
450 legend('Reconstrued projection','Initial projection')
```